J. Fluid Mech. (1980), *vol.* 101, *part* 1, *pp.* 129–158
Printed in Great Britain

Full-coverage film cooling. Part 1. Three-dimensional measurements of turbulence structure

By S. YAVUZKURT, R. J. MOFFAT AND W. M. KAYS

Mechanical Engineering Department, Stanford University, CA 94305

(Received 31 January 1979 and in revised form 29 January 1980)

Hydrodynamic measurements were made with a triaxial hot wire in the full-coverage region and the recovery region following an array of injection holes inclined downstream, at 30° to the surface. The data were taken under isothermal conditions at ambient temperature and pressure for two blowing ratios: $M = 0{\cdot}9$ and $M = 0{\cdot}4$. (The ratio $M = \rho_{\text{jet}} U_{\text{jet}} / \rho_\infty U_\infty$, where U is the mean velocity and ρ is the density. Subscripts jet and ∞ stand for injectant and free stream, respectively.) Profiles of the three mean-velocity components and the six Reynolds stresses were obtained at several spanwise positions at each of five locations down the test plate.

In the full-coverage region, high levels of turbulence kinetic energy (TKE) were found for low blowing and low TKE levels for high blowing. This observation is especially significant when coupled with the fact that the heat transfer coefficient is high for high blowing, and low for low blowing. This apparent paradox can be resolved by the hypothesis that entrainment of the mainstream fluid must be more important than turbulent mixing in determining the heat transfer behaviour at high blowing ratios (close to unity).

In the recovery region, the flow can be described in terms of a two-layer model: an outer boundary layer and a two-dimensional inner boundary layer. The inner layer governs the heat transfer.

1. Introduction

There have been many studies of heat transfer with film cooling. One general review is given by Goldstein (1971), and another by Choe, Kays & Moffat (1975). Most of the early experimental research on full-coverage film cooling concentrated on measurement of film-cooling effectiveness, assuming the heat-transfer coefficients to be known. The hydrodynamics was treated as secondary in importance. A review of the experimental work on this topic is also given by Crawford, Kays & Moffat (1976).

Le Brocq, Launder & Priddin (1971) studied the effects on film-cooling effectiveness, η, of hole-pattern arrangement, injection angle, ratio of densities of the coolant and mainstream, and blowing ratio. Some profiles of mean velocity were taken near the holes, with a Pitot probe. The staggered hole pattern was found to be more effective than the in-line pattern and slant-angle injection was found to be more effective than the normal injection. An optimum blowing ratio was found which gave maximum effectiveness; above the optimum blowing ratio, effectiveness decreased again.

0022-1120/80/4534-2300 $02.00

Launder & York (1974) studied the effects of mainstream acceleration and turbulence level on film-cooling effectiveness, using a staggered 45° slant-hole test section. Acceleration seemed to increase effectiveness, but the free-stream turbulence did not have a significant effect. A small number of mean velocity profiles were taken.

Metzger, Takeuchi & Kuenstler (1973) studied both effectiveness and heat transfer on a full-coverage surface with normal holes spaced 4·8 diameters apart, arranged in both in-line and staggered patterns. They confirmed that a staggered pattern was more effective. No hydrodynamic measurements were made.

Mayle & Camarata (1975) examined the effects of hole spacing P and blowing ratio on heat transfer and film effectiveness for a staggered-hole array with compound-angle injection. It was found that for $P/D = 10$ and 8 (where D is the hole diameter of the injection tube) higher effectiveness was obtained than with $P/D = 14$. No measurements were made of the hydrodynamics of the flow field.

Very little of the literature mentioned above gives any information about flow-field measurements and, in particular, measurements of turbulence quantities. In the following papers, however, some attempts were made to make measurements of hydrodynamics.

Choe *et al.* (1975) studied the effects on hydrodynamics and heat transfer of hole spacing, blowing ratio, mainstream velocity and conditions upstream of the discrete-hole array. Normal injection was used with a staggered array of holes spread 5 and 10 diameters apart. Mean velocity profiles were taken with Pitot probe and used to obtain spanwise-averaged values. From the spanwise-averaged profile, a mixing-length distribution was obtained and later used in predictions of heat-transfer data with a one-equation model of turbulence.

Ramsey & Goldstein (1971) measured the mean velocity and turbulence intensity profiles (not the turbulent kinetic energy) downstream of a heated jet at blowing ratios of 1·0 and 2·0 for normal injection. Metzger, Carper & Warren (1972) measured the mean velocity profiles both upstream and downstream of a two-dimensional injection slot. Hartnett, Birkebak & Eckert (1961) measured boundary-layer velocity profiles for a number of positions downstream of injection through a single slot. Foster & Haji-Sheikh (1974) measured mean velocities downstream of flush, normal-injection slots.

The heat-transfer studies reported in the preceding paragraphs have pointed out some important characteristics of discrete-hole injection which can only be explained by hydrodynamic measurements: the existence of an optimum blowing ratio, the effect of acceleration on surface effectiveness, the effect of free-stream turbulence on surface effectiveness, and the effect of pitch-to-diameter ratio. It seems likely that the key to the understanding of these phenomena lies in the detailed turbulence structure of the flow in the full-coverage and in the recovery regions.

In the present work, measurements were made of the turbulence structure and mean velocity field in the turbulent boundary layer in the full-coverage film-cooled region and in the recovery region. The objective was to obtain sufficient data to permit development of adequate models for the spanwise-averaged (i.e. quasi-two-dimensional) behaviour of the turbulent boundary layer with full-coverage film cooling.

2. Experimental apparatus and instrumentation

The full-coverage film-cooling test rig is a closed-loop wind tunnel using air at ambient pressure and temperature, previously used by Choe *et al.* (1975) and Crawford *et al.* (1976). It is described in detail in their work. Only those aspects relevant to the present research are given here.

2.1. *The test surface*

The test surface has three parts: a preplate, a full-coverage region, and an afterplate.

The preplate is made of 24 individual copper plates, each about 2·6 cm long in the flow direction and 46 cm wide, assembled to form a smooth surface.

The full-coverage section is composed of 12 copper plates, each 0·6 cm thick, 46 cm wide, and 5 cm long in the flow direction. The first plate does not have any holes, but the remaining 11 have alternately nine and eight holes in each. The holes are 1·03 cm in diameter and are spaced on five-diameter centres to form a staggered-hole array. A photograph of the full-coverage section can be seen in figure 1 (plate 1). Each plate segment is individually instrumented to allow measurement of the spanwise-averaged heat transfer and the injection flow rate. Delivery tubes for secondary air extend beneath the surface at a 30° angle to the plate surface.

The afterplate is identical with the preplate. This is the recovery region for the flow, downstream of the blown part of the test section. Crawford *et al.* (1976) give detailed information about the test surface.

The main instrumentation for the present experiments was the hot-wire system used in the measurements of the turbulent flow field. It consists of a DISA claw-type triaxial hot-wire probe, three constant-temperature anemometers (TSI 1050), three polynomial linearizers (TSI 1052), and an analog device for real-time data reduction (3-D Turbulent Flow Analyzer). Detailed information about the hot-wire instrumentation, calibration, and the qualification of the measurement technique is given in Yavuzkurt, Moffat & Crawford (1977*b*).

Tabular data listings and details of the measurement techniques and instrumentation are given by Yavuzkurt, Moffat & Kays (1977*a*).

2.2. *The experimental conditions*

The experiments were made under isothermal conditions, with air temperatures around 22–25 °C. The pressure levels were about atmospheric ($\sim$ 760 mm of mercury), and the experiments were made at a uniform free-stream velocity of approximately 16 m s^{-1}. The velocity of the free stream was kept uniform along the test section by adjusting the top wall (as explained in Crawford *et al.* 1976), so that the static pressure change along the tunnel was less than $\pm$ 0·8 % of free-stream dynamic head ($\pm$ 0·13 mm of water). The free-stream and jet turbulence levels ($(q^2)^{\frac{1}{2}}/U_\infty$) were 0·008 and 0·050, respectively. The turbulent kinetic energy $q^2 = \overline{u'^2} + \overline{v'^2} + \overline{w'^2}$, where $\overline{u'^2}$ is the Reynolds normal stress in the x direction, etc.

Experiments were made at two different blowing ratios, $M = 0{\cdot}4$ and $M = 0{\cdot}9$. The $M = 0{\cdot}4$ ratio was chosen because Crawford *et al.* (1976) showed it to result in minimum Stanton number, while $M = 0{\cdot}9$ displayed definitely different behaviour.

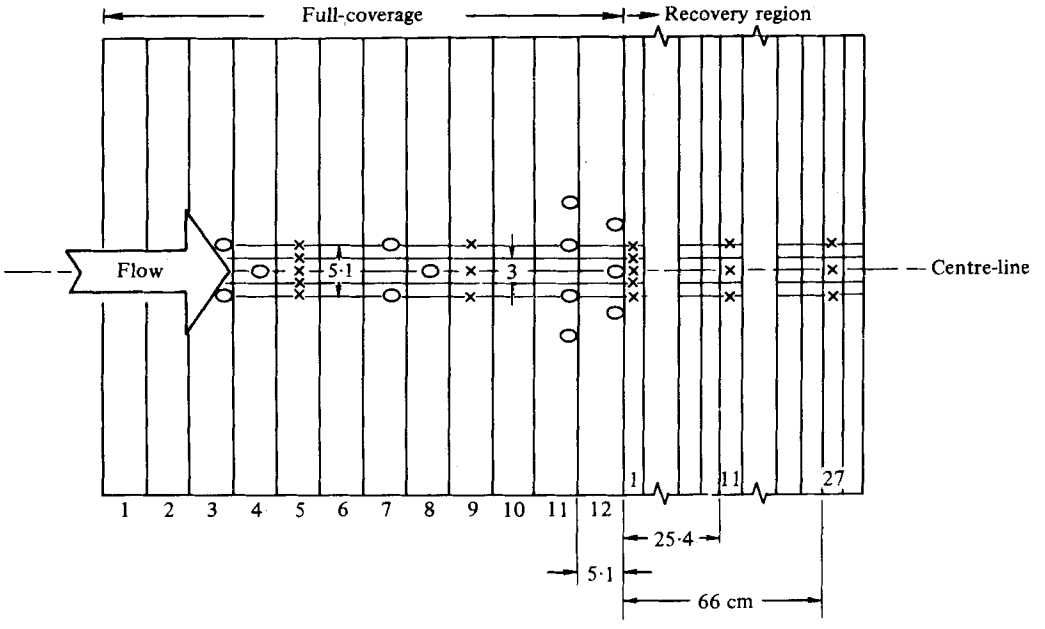

FIGURE 2. Measurement locations.

2.3. *The measurement locations*

The measurement locations can be seen in figure 2. Five streamwise positions were selected for measurements to observe the development of the flow field on the full-coverage surface and its relaxation in the recovery region. The first was located at the centre of the 5th plate of the full-coverage region (at $x = 148$ cm) after three rows of blowing. The second was at the centre of the 9th plate ($x = 168$ cm) after seven rows of blowing in the full-coverage region. The third one was at the centre of the first plate in the recovery region ($x = 188$ cm) after 11 rows of blowing. The last two are at the centres of the 11th ($x = 214$ cm) and 27th plates ($x = 256$ cm) in the recovery region and are, respectively, 27 and 67 hole diameters downstream from the last row of injection holes. Several measurements were made at each streamwise position in order to see spanwise variations in the flow. At the first and third stations, five spanwise locations were used, $+0{\cdot}5$, $+0{\cdot}3$, 0, 0, $-0{\cdot}3$ and $-0{\cdot}5$. The flow field was periodic and repeated itself after $z/P = +0{\cdot}5$ and $-0{\cdot}5$. At the second streamwise location three spanwise locations were selected at $z/P = +0{\cdot}5$, 0 and $-0{\cdot}5$. In the recovery region for $M = 0{\cdot}9$, at each streamwise location, three spanwise locations were used. After the experiments at $M = 0{\cdot}9$, it was seen that the profiles in the recovery region were the same in all three spanwise locations, as illustrated by figures 5 and 10. So for $M = 0{\cdot}4$ these spanwise locations were eliminated in the recovery region. The profiles were used to obtain the necessary spanwise-averaged input to the two-dimensional boundary-layer program STAN5 (Crawford & Kays 1975). Measurements were made at each location of the three mean velocities and the six Reynolds stresses.

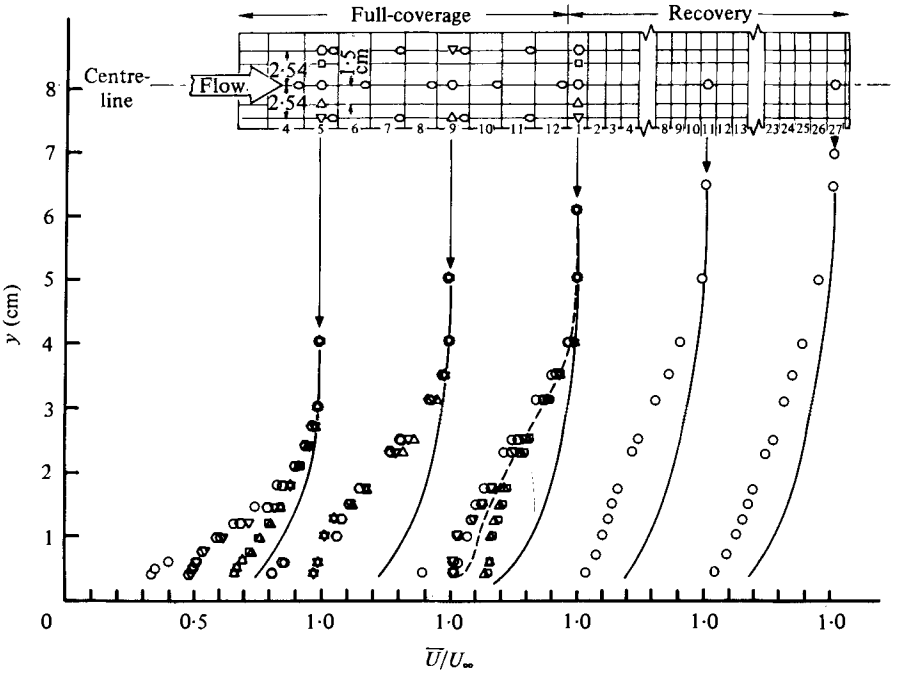

FIGURE 3. Profiles of the streamwise mean velocity component, $\overline{U}$, for $M = 0{\cdot}4$; $U_\infty = 16{\cdot}5$ m s^{-1}. – – –, spanwise average; ——, $\frac{1}{7}$ profile.

3. Results and discussion

In this section attention will be given to the streamwise component of the mean velocity, $\overline{U}$, rather than discussing the three-dimensionality of the flow around the holes. (Throughout, the overbar denotes the time-averaged value.) Two sets of profiles for different blowing ratios will be discussed and compared with each other.

3.1. *Mean velocity profiles for* $M = 0{\cdot}4$

Figure 3 shows the mean velocity profiles at each spanwise location, at each of the five streamwise stations, for the blowing ratio $M = 0{\cdot}4$. The location of each of the traversing stations is marked on each figure with respect to the injection locations.

The first observation on this figure is the remarkable symmetry of the profiles with respect to the centre-line. There is a definite periodicity in the spanwise direction, and the coalescing of the upstream jets is regular.

In the full-coverage section, two distinct regions appear in each profile. In the outer region all spanwise profiles are the same; in the inner region, differences are observed related to the injection. The same observation was made by Le Brocq *et al.* (1971) for a 45° injection. The spanwise profiles have other systematic characteristics as well. The central profiles just downstream of a jet show the greatest velocity defect, because they are affected directly by injection. The profiles at the outer edges of a hole show less defect than the central profile but more defect than the intermediate positions, which are between two holes. The outer profiles are affected by the injection one row upstream and are still recovering from the effect of that injection, while the profiles between two holes have no injection in line with them and are affected only by the

lateral spreading of jets. This is clearly seen in figure 3, where, after three rows of blowing, the intermediate profiles show almost no defect, thus indicating that the effect of lateral spreading has not reached them with its full force yet. After 11 rows of blowing, however, the momentum defect in the intermediate profiles can easily be observed.

The velocity defect region, with respect to a two-dimensional profile, extends nearly twice as far from the wall after 11 rows of blowing as after three rows, as shown in figure 3. This indicates the cumulative effect of upstream jets which keep rising as they spread downstream. The jets penetrate only about 2 cm immediately after injection, as can be seen from the abrupt change in the slope of the profiles, about two jet diameters for this blowing ratio. The mass shed into the boundary layer by each injection row penetrates to an almost constant distance, for a certain blowing ratio, before the jets are knocked down by the mainstream. The immediate penetration distance increases slightly as one goes downstream, since the boundary layer loses momentum due to the effect of previous injections. This constant penetration distance was also observed by Le Brocq *et al.* (1971), Crawford *et al.* (1976), Colladay & Russell (1975) and Ramsey & Goldstein (1971).

There is no indication of reverse flow or of separation of the jets from the surface, but this might be because the profiles were measured at locations where the jets have already reattached. The measurement locations were 2·5 hole diameters downstream from the edge of the closest hole. Separation of the jets from the surface was observed by Bergeles, Gosman & Launder (1975) for normal blowing at a blowing ratio of $M = 0{\cdot}24$, but extended only to 1·5 diameters downstream of the hole. It is generally agreed in the literature (Le Brocq *et al.* 1971; Colladay & Russell 1975) that slant-injection jets stay attached to the surface to much higher blowing ratios than for normal injection. Launder & York (1974) state that for a 45° in-line injection with $P/D = 8$, the jets attach to the surface at 3–4 hole diameters downstream of the last injection for $M = 0{\cdot}6$. These observations help one arrive at the conclusion that the jets for the 30° slant injection for $M = 0{\cdot}4$ may reattach to the surface in a very short distance downstream, or perhaps don't separate at all.

The points which are closest to the wall in all the mean velocity profiles have almost the same value of $\overline{U}/U_\infty$ for the same spanwise locations at all streamwise stations. For the central profiles the value is $\overline{U}/U = 0{\cdot}35$–$0{\cdot}4$. This is close to the value of the blowing ratio ($\overline{U}_{\rm jet}/U_\infty = 0{\cdot}4$) multiplied by the cosine of the injection angle (30°), a definite indication of the importance of the average jet velocity in the near-wall region. It was observed by Bergeles *et al.* (1975) that the velocity in the exit plane of jets is not uniform, but even so the effect seems governed by the average jet velocity, given by $M \times U_\infty$.

In figure 3, curves representing $\frac{1}{7}$-power profiles are shown as reference lines to make comparisons easier. It was expected that, finally, in the recovery region, the boundary layer would return to a normal two-dimensional, flat-plate boundary layer. A spanwise-averaged profile is also shown for the profiles at the start of the recovery region. When compared to the $\frac{1}{7}$-power profiles, it can be seen that the momentum defect decreases as the boundary layer recovers from the blowing. However, there is a considerable momentum deficit even at the last recovery-region station, due to the large initial deficit. The reason for the long recovery distance is the 'momentum-sink' action of the wall. Diffusion of momentum from the free stream is the only way for

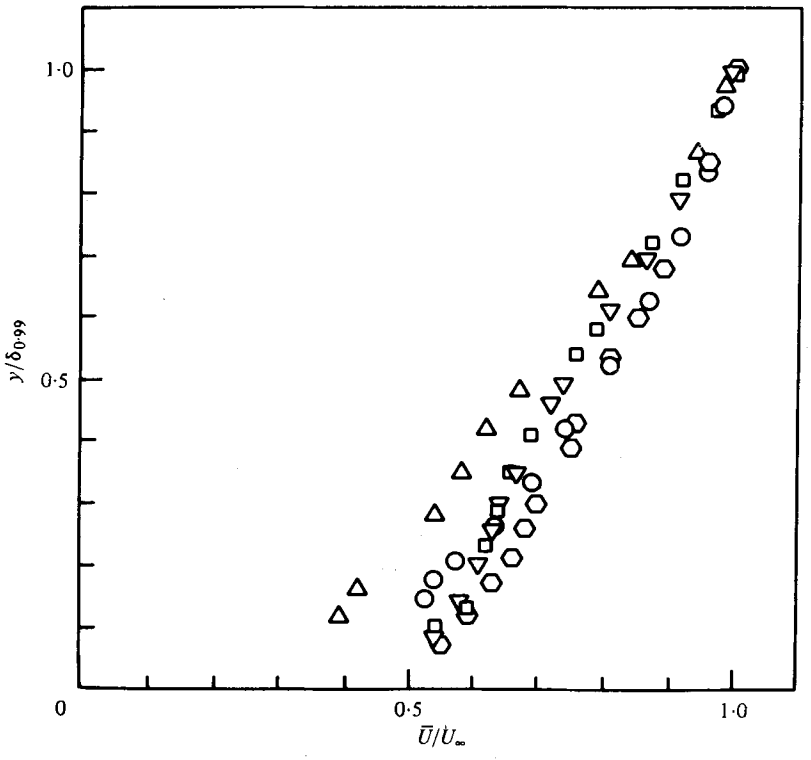

FIGURE 4. Spanwise-averaged profiles of the streamwise mean velocity component, $\bar{U}$, for $M = 0{\cdot}4$; $U_\infty = 16{\cdot}5$ m s^{-1}. ○, $x = 148$; △, $x = 168$; □, $x = 188$; ▽, $x = 214$; ⬡, $x = 256$.

these profiles to recover to two-dimensional flat-plate profiles, and diffusion is a slow process. The long recovery distance indicates that the effects of jets near the wall prevail over long distances for low blowing.

Velocity gradients at the wall are smaller than for a two-dimensional flat-plate profile; this will give lower friction factors. There is also no indication of boundary-layer separation except locally at the injection points. Thus, the aerodynamic behaviour of the 30° slant-hole in-line injection with $M = 0{\cdot}4$ is quite good. Since this blowing also gives the lowest heat-transfer coefficients (Crawford *et al.* 1976), it is a very important blowing ratio in full-coverage film-cooling applications. Le Brocq *et al.* (1971) agree with this conclusion.

Figure 4 shows the spanwise-averaged mean velocity for $M = 0{\cdot}4$ in y/δ and $\bar{U}/U_\infty$ co-ordinates; δ is the boundary-layer thickness. The profile at $x = 168$ cm is not to be trusted quantitatively near the wall. Only three spanwise profiles were taken at this location, and the spanwise averaging of three profiles does not represent a physically correct average. It is plotted here, however, for comparisons in the outer layers, where the spanwise profiles are not very different from each other, and the resulting average is correct. The profile after three rows of blowing ($x = 148$ cm) has the largest momentum defect, but the difference from the others is not great. The region near the wall is governed by the latest injection and stays almost at the same level of $\bar{U}/U_\infty$. The effects of previous rows can be seen in the outer layers. For example, in the outer regions, the profile at $x = 148$ cm is very close to the profile at the last

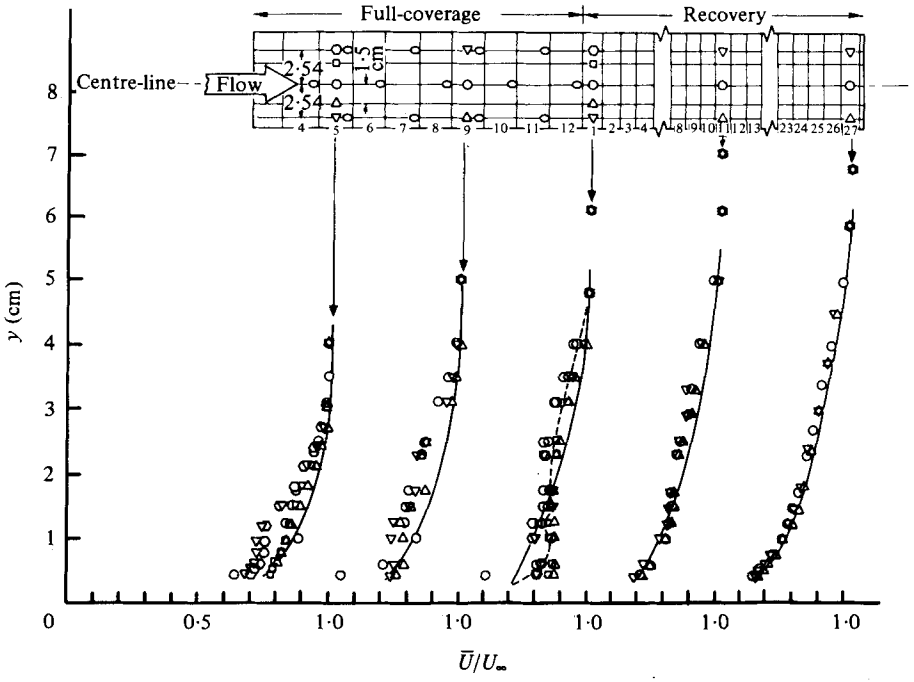

FIGURE 5. Profiles of the streamwise mean velocity component, $\bar{U}$, for $M = 0{\cdot}9$; $U_\infty = 16{\cdot}7$ m s^{-1}. – – –, spanwise average; ——, $\frac{1}{7}$ profile.

recovery station ($x = 256$ cm). The jets cannot strongly affect the outer layers at this distance. The outer region profiles are very similar after 7 and 11 rows of blowing ($x = 168$, 188 cm, respectively) and in the recovery region profile at 27 hole diameters downstream of the last row of injection ($x = 214$ cm). The result of these observations can be summarized as follows: after four or five rows of blowing it appears that the boundary layer reaches a state of equilibrium over a large part of the layer (almost above $y/\delta \geqslant 0{\cdot}1$) for low blowing. This may be very helpful in the modelling of the injection process in the full-coverage region.

3.2. *Mean velocity profiles for* $M = 0{\cdot}9$

Figure 5 shows the spanwise mean velocity profiles at five streamwise locations for the blowing ratio of $M = 0{\cdot}9$. Spanwise symmetry can be observed, as in $M = 0{\cdot}4$. This indicates uniform lateral jet spread. Nina & Whitelaw (1971) cautioned against non-uniform coalescing of jets in full-coverage film-cooling applications; such a phenomenon was not observed here.

Again, two distinct regions can be observed in the profiles: outer and inner. In the outer region all the spanwise profiles are the same at each streamwise station. In the inner region, however, there are differences in the profiles which depend on the spanwise location. The size of the inner region is very large compared to the $M = 0{\cdot}4$ case because of the higher rate of blowing and deeper penetration of the jets. The jets penetrate to approximately three hole diameters (~ 3 cm) at $M = 0{\cdot}9$, for all the stations.

Another difference between the cases is the excess momentum near the wall in

$M = 0{\cdot}9$ because of the high blowing ratio. This can be observed by comparing the spanwise-averaged profile to the $\frac{1}{7}$-power reference curve at the third streamwise location.

In the central profiles just downstream of a jet, a local maximum in velocity occurs around $y = 1$ cm with $\overline{U}/U_\infty = 0{\cdot}85$–$0{\cdot}9$ (this was not observed for $M = 0{\cdot}4$). This point is the centre-line of the recently injected jet, about one hole diameter above the surface. This can be observed at the same location in every station of the full-coverage region. This maximum in the streamwise mean velocity was also observed by LeBrocq *et al.* (1971) for $M = 0{\cdot}5$ and $P/D = 8$ for 45° injection. This is another indication of the fact that the depth of immediate penetration is constant.

It is important to observe that, at the point closest to the wall in the central profiles, there is a sharp decrease in the velocity. This indicates that the jet has separated from the surface and has not yet reattached at the measurement location (about 2·5 diameters downstream of the hole). This phenomenon is not observed in the side profiles, which are 7·5 hole diameters away from the last injection location. Therefore, it can be concluded that, for the case of $M = 0{\cdot}9$, the jets reattach to the surface somewhere between 2·5 and 7·5 hole diameters downstream of their injection location. This was also observed by Colladay & Russell (1975) and by Launder & York (1974). The separation of the protective jet from the surface helps explain the high heat transfer coefficients of the $M = 0{\cdot}9$ case reported by Crawford *et al.* (1976). The spanwise-averaged mean velocity profile has a region of negative slope which gives rise to a locally negative shear stress.

There is a rapid relaxation back to the two-dimensional state in the recovery region, as can be seen from the comparison of the profiles in this region with $\frac{1}{7}$-power profiles. In fact, the profile at the last recovery region station is almost the same as the $\frac{1}{7}$ profiles, except for a small momentum deficit in the outer layer. Relaxation back to the two-dimensional state is much faster for $M = 0{\cdot}9$ than for $M = 0{\cdot}4$ because there is excess momentum near the wall. The wall, acting as a momentum sink, facilitates the relaxation process. In the outer layer, where there is some momentum deficit, the relaxation process is very slow. The momentum supplied by the free-stream entrainment and by diffusive transport does not permit rapid relaxation.

Higher velocity gradients near the wall (when compared with the $\frac{1}{7}$ profile and the $M = 0{\cdot}4$ profiles) lead to larger skin-friction coefficients, thus increasing the aerodynamic drag. Increase in the skin-friction coefficient with blowing was observed by Kacker & Whitelaw (1970) for a two-dimensional wall jet.

One observes generally the lack of velocity gradient all over the $M = 0{\cdot}9$ mean profiles except at the wall. This yields low shear stresses and low turbulent kinetic energy (TKE) throughout a large part of the boundary layer. Samuel & Joubert (1965) observed that, the closer the M is to unity, the lower the turbulent mixing is for a two-dimensional injection. Seban & Back (1962) made the same observation in the case of a two-dimensional tangential injection.

In figure 6, spanwise-averaged profiles for five streamwise locations are plotted on y/δ and $\overline{U}/U_\infty$ co-ordinates for $M = 0{\cdot}9$. A very clear outer-layer similarity is observed in these co-ordinates; the profiles lie much closer to each other than for $M = 0{\cdot}4$. The similarity is not observable below $y/\delta = 0{\cdot}25$, perhaps because the high rate of blowing causes non-equilibrium in that region. Another indication of non-equilibrium can be seen in figure 5. The intermediate profiles in each streamwise location continue

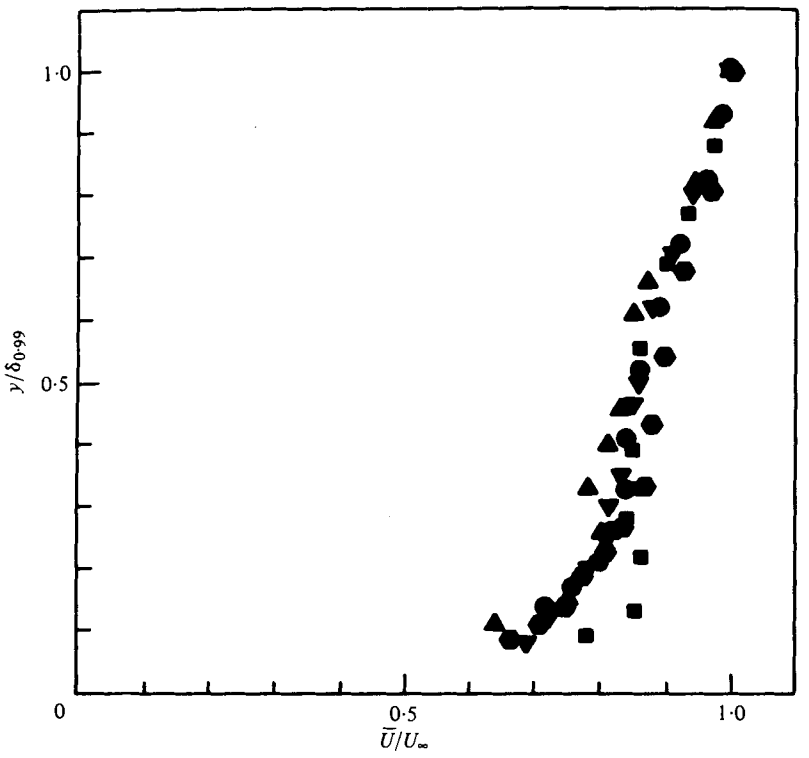

FIGURE 6. Spanwise-averaged profiles of the streamwise mean velocity component, $\overline{U}$, for $M = 0{\cdot}9$; $U_\infty = 16{\cdot}7$ m s^{-1}. ●, $x = 148$; ▲, $x = 168$; ■, $x = 188$; ▼, $x = 214$; ⬢, $x = 256$.

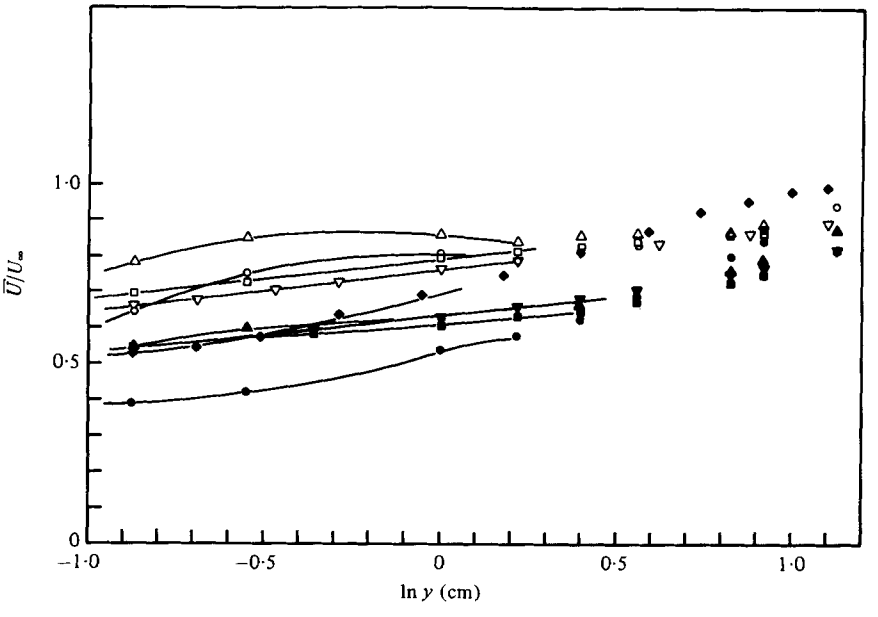

FIGURE 7. Spanwise-averaged profiles of the streamwise mean velocity component, $\overline{U}$, plotted in semi-log co-ordinates. Open symbols are for $M = 0{\cdot}9$, solid symbols are for $M = 0{\cdot}4$. ◇, $x = 148$; ○, $x = 168$; △, $x = 188$; □, $x = 214$; ▽, $x = 256$.

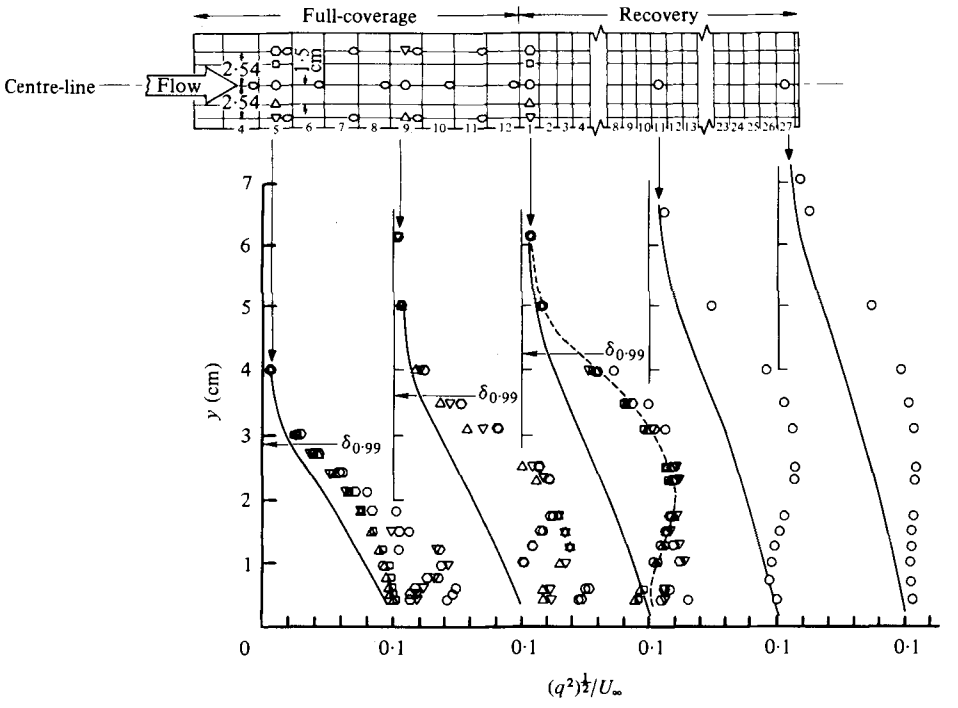

FIGURE 8. Turbulent kinetic energy profiles for $M = 0{\cdot}4$; $U_\infty = 16{\cdot}5$ m s^{-1}. – – –, spanwise average; ——, two-dimensional flat-plate TKE.

to get fuller with each downstream location; they do not reach an equilibrium even after 11 rows of blowing.

Figure 7 shows the spanwise-averaged mean velocity components in semi-logarithmic co-ordinates ($\bar{U}/U_\infty$ *vs.* $\ln y$) for $M = 0{\cdot}4$ and $M = 0{\cdot}9$. No logarithmic region can be seen in the profiles for either case, in the full-coverage region. The signs of the curvatures of the profiles in the full-coverage region are opposite for different blowing ratios; this is an indication of the momentum deficit in one case and of the momentum excess in the other. In the recovery region, however, there is a definite indication of a logarithmic region near the wall. The two profiles at $x = 214$ cm and $x = 256$ cm exhibit linear regions for both blowing ratios; this proves that, as soon as the blowing steps, wall effects are dominant and the 'law of the wall' seems to apply.

3.3. *Turbulent kinetic energy profiles for* $M = 0{\cdot}4$

Figure 8 shows the TKE profiles at several spanwise locations at each of five streamwise stations for $M = 0{\cdot}4$. Spanwise symmetry can be observed in these profiles, indicating an orderly behaviour of the turbulent flow field.

In the full-coverage region, there is a strong convergence in the TKE profiles above $y = 2$ cm at all spanwise locations, but large differences exist between the profiles below $y = 2$ cm. This relates to the 2 cm penetration distance and indicates that only the region near the wall is locally affected by the jets.

Near the wall, the highest TKE is observed in the central profiles; the second highest in the side profiles. The intermediate profiles have the lowest TKE, as expected (no

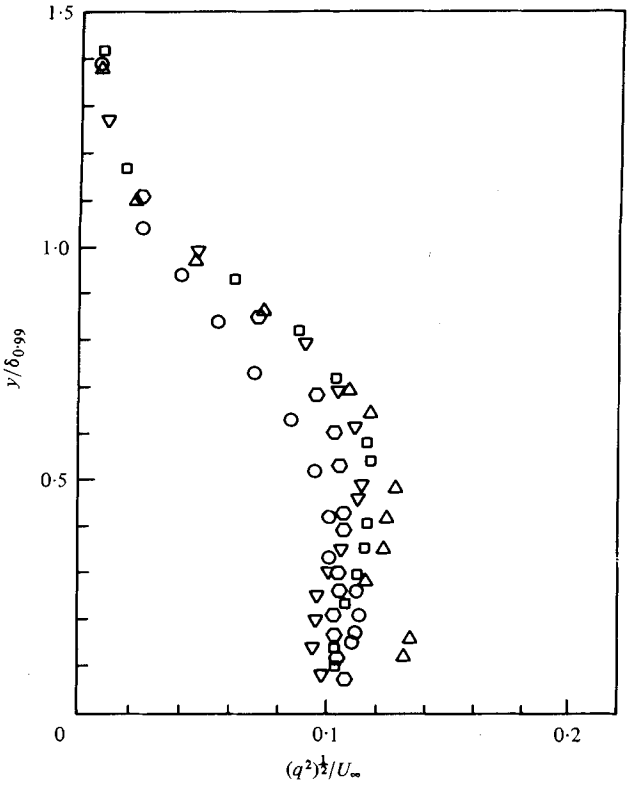

FIGURE 9. Spanwise-averaged turbulent kinetic energy profiles for $M = 0{\cdot}4$; $U_\infty = 16{\cdot}5$ m s^{-1}. ○, $x = 148$; △, $x = 168$; □, $x = 188$; ▽, $x = 214$; ⬡, $x = 256$.

jets are in line with them). There is a dip in the centre profiles around $y = 1$ cm, which can be explained as follows. There is a high-velocity gradient near the wall which causes high shear, resulting in higher TKEs in that vicinity. However, there exists a region of very low velocity gradient (see figure 3) just above it, because of injection. In this region, the local TKE production is decreased but local dissipation is high, leading to low TKE values. The low-velocity gradient region ends at about $y = 2$ cm (penetration distance). Above this level, higher-velocity gradients lead to higher TKE. As a result, a double maximum is observed in the central TKE profiles. The side TKE profiles have only one maximum. At some distance from the injection location, the TKE near the wall dissipates and the maximum near the wall vanishes. TKE diffuses from the second maximum towards the wall, resulting in a smooth profile with one maximum.

In figure 8, profiles of turbulence kinetic energy typical of two-dimensional, flat-plate layers are also shown, as references for comparison. The flat-plate TKE profiles were obtained with the STAN5 computer program (Crawford & Kays 1975) for the same free-stream turbulence level as the experimental profiles. A spanwise-averaged TKE profile is shown at the start of the recovery region. Comparisons with the two-dimensional profile show that there is excess TKE throughout the region, but that most of the excess energy lies in the middle section of the boundary layer. Even though the jets do not penetrate very far into the boundary layer, the TKE diffuses towards

the free stream, causing large TKE values far from the wall. In the recovery region, there is still high TKE compared to the two-dimensional value.

The high TKE (turbulent mixing) levels in the recovery region are felt to be the reason for the slowly rising Stanton numbers here for $M = 0{\cdot}4$. Crawford *et al.* (1976) observed that Stanton numbers for $M = 0{\cdot}4$ decrease in the full-coverage region and rise slowly in the recovery region. This process can be explained in terms of the TKE levels, as follows. The TKE levels are higher than the two-dimensional boundary-layer values, which should cause high Stanton numbers; however, at the same time, an energy sink has been created in the full-coverage region by the cold injection. The combination of these two opposing phenomena results in the low and decreasing Stanton numbers in the full-coverage region. There is no injection in the recovery region (i.e. the energy sink is not being replenished), but the turbulence level (turbulent mixing) is still high. The mixing process, unopposed, increases the Stanton numbers, and they rise gradually in the recovery region.

In figure 9, spanwise-averaged TKE profiles are plotted in y/δ and $(q^2)^{\frac{1}{2}}/U_\infty$ coordinates for each streamwise station. There is no definite similarity in any region, even though all the profiles seem very similar (again, for the $x = 168$ cm profile, the points near the wall are to be neglected). There is an indication of invariance in the TKE profiles in the full-coverage region after four or five rows of blowing (over $y/\delta = 0{\cdot}1$), as was true of the streamwise mean velocity profiles.

3.4. *Turbulent kinetic energy profiles for* $M = 0{\cdot}9$

Figure 10 shows the TKE profiles for several spanwise locations at each of five streamwise stations for $M = 0{\cdot}9$.

Spanwise symmetry can be observed in the profiles, within the experimental uncertainty limits.

The behaviour of the TKE is qualitatively similar to the $M = 0{\cdot}4$ case – as opposed to the mean velocity profiles, which exhibited different behaviour. Once more, the highest TKE lies in the central profiles, the next highest in the side profiles, and the lowest in the intermediate profiles. However, quantitatively, there are large differences between the TKE profiles for the $M = 0{\cdot}4$ case and the $M = 0{\cdot}9$ case.

The double maximum observed in the $M = 0{\cdot}4$ TKE profiles is not found here. The highest TKE occurs next to the wall rather than in the outer region, owing to the high velocity gradient there. Above $y = 2{\cdot}0$ cm, there is a sharp drop in TKE. Also, the TKE levels for $M = 0{\cdot}9$ are much lower than in the case of $M = 0{\cdot}4$ within a large region of the boundary layer outboard of $y/\delta \cong 0{\cdot}15$ (compare the spanwise-averaged profile at the start of the recovery region with the two-dimensional TKE profile). This is clear evidence of a decrease in turbulence level as the blowing ratio approaches 1. The TKE levels are lower because of the low velocity gradients in the $M = 0{\cdot}9$ case. This behaviour may be due primarily to the dependence of the TKE production on the mean velocity gradient – the larger the mean velocity gradient, the larger the TKE production and the TKE itself.

The lower TKE levels for the higher blowing case seem, at first glance, to be inconsistent with the heat-transfer data obtained by Crawford *et al.* (1976), but when examined closely it can be seen that there may be an explanation: the governing process for the heat transfer may be different. Crawford *et al.* (1976) observed that the Stanton number for the $M = 0{\cdot}9$ case is below the two-dimensional flat-plate value

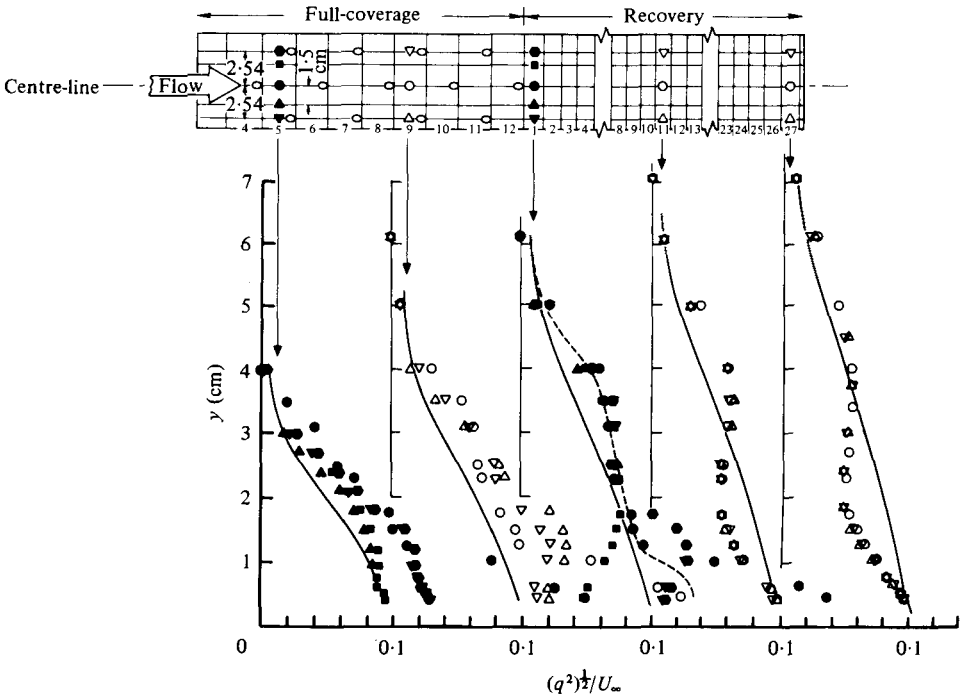

FIGURE 10. Turbulent kinetic energy profiles for $M = 0{\cdot}9$; $U_\infty = 16{\cdot}7$ m s^{-1}. – – –, spanwise average; ——, two-dimensional flat-plate TKE.

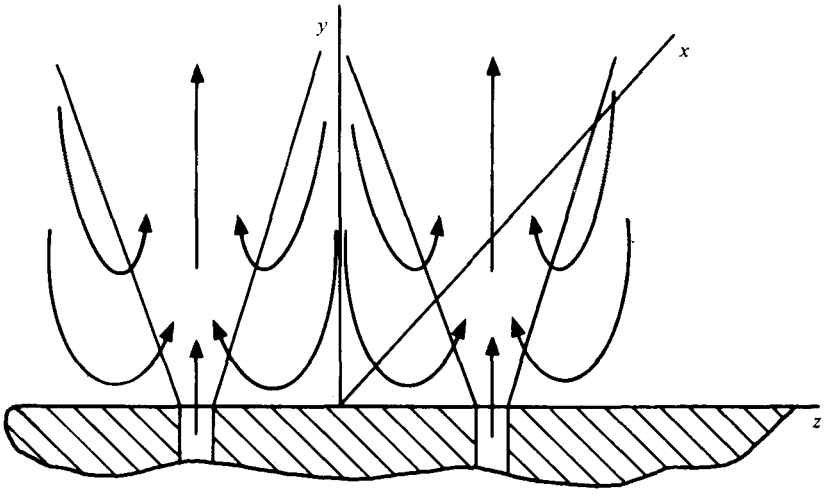

FIGURE 11. Schematic diagram of the entrainment process for high blowing ratios.

but above the value for the $M = 0{\cdot}4$ case, when the injected fluid is at the same temperature as the plate. The Stanton-number values decreased in the downstream direction in the full-coverage region and also in the recovery region. If turbulent mixing were the governing process in the heat transfer, one would expect the Stanton numbers for the $M = 0{\cdot}9$ case to be lower than for the $M = 0{\cdot}4$ case, for two reasons:

first, more cold fluid is injected into the boundary layer for high blowing and, secondly, there is less turbulent mixing. Instead, higher Stanton numbers were observed. The main reason could be that, for high blowing, the jets separate from the wall and penetrate deeply into the boundary layer, entraining hot free-stream fluid towards the wall in the middle lanes. This process is schematically explained in figure 11. This figure was also used by Le Brocq *et al.* (1971) to describe the in-line blowing process. The present results suggest that this same process occurs in a staggered array, at high blowing. This hypothesis is also supported by the $\overline{V}$ component of the mean velocity, as can be seen in figures 17 and 18.

In addition to the entrainment process, another mechanism is at work – the cold fluid (energy sink) is being deposited in the outer layer, due to the separation of the jets from the surface.

In summary, two different pairs of opposing processes seem to control the heat transfer: (i) high turbulent mixing with an energy sink near the wall, for low blowing; and (ii) outer-layer fluid entrainment with an energy sink in the outer layer, for high blowing.

In the recovery region, the Stanton numbers continue to decrease because the entrainment of the outer-layer fluid stops immediately, but the energy sink is still there.

In figure 10, the recovery region TKE profiles are compared with two-dimensional flat-plate TKE profiles. The behaviour of the TKE is very interesting. At the start of the recovery region, the spanwise-averaged TKE is higher than the two-dimensional value; however, by 27 hole diameters into the recovery region, the TKE values are lower than the two-dimensional value below $y \simeq 3$ cm. The derivation from the two-dimensional value increases in the downstream direction, although one would expect it to decrease. This can be explained as follows. Figure 5 shows that the spanwise-averaged mean-velocity profile at the start of the recovery region has negative velocity gradients close to the wall. There are also negative shear stresses in the same area, as seen in figure 14. In fact, since the flow is three-dimensional, there are y locations where the mean velocity gradient is positive and the shear stress negative, and vice versa. This results in the apparent negative production of TKE. The high TKE near the wall is dissipated rapidly as soon as the injection stops and thus cannot feed the low TKE regions by diffusion. As a result of the 'negative production', the dissipation, and the decreased diffusion, the TKE falls below the two-dimensional flat-plate value. Even though the negative velocity gradient region diminishes rapidly after the last row of injection, its effect on TKE continues because the turbulence profiles respond slowly to changes. The production first becomes zero and then positive. A considerable distance is required before the production begins once more to increase the TKE level.

The relaxation of TKE in the recovery region occurs in the expected direction in the outer layer. This rate is again slow, as can be observed in the $M = 0{\cdot}4$ case. In the near-wall region, TKE responds rapidly. At the point nearest the wall, TKE drops quickly from $(q^2)^{\frac{1}{2}}/U_\infty = 0{\cdot}134$ to $0{\cdot}1$, after the last row of injection, and remains at that level throughout the recovery region. This is also true for $M = 0{\cdot}4$, in the recovery region (see figure 8) for a two-dimensional flat-plate boundary layer. These observations illustrate the rapid recovery to the two-dimensional state in the near-wall layer ($y/\delta \leqslant 0{\cdot}1$), which occurs as soon as the injection stops.

Figure 12 shows the spanwise-averaged TKE profiles for $M = 0{\cdot}9$ at four streamwise stations (the $x = 168$ cm data have been discarded, as discussed earlier). There

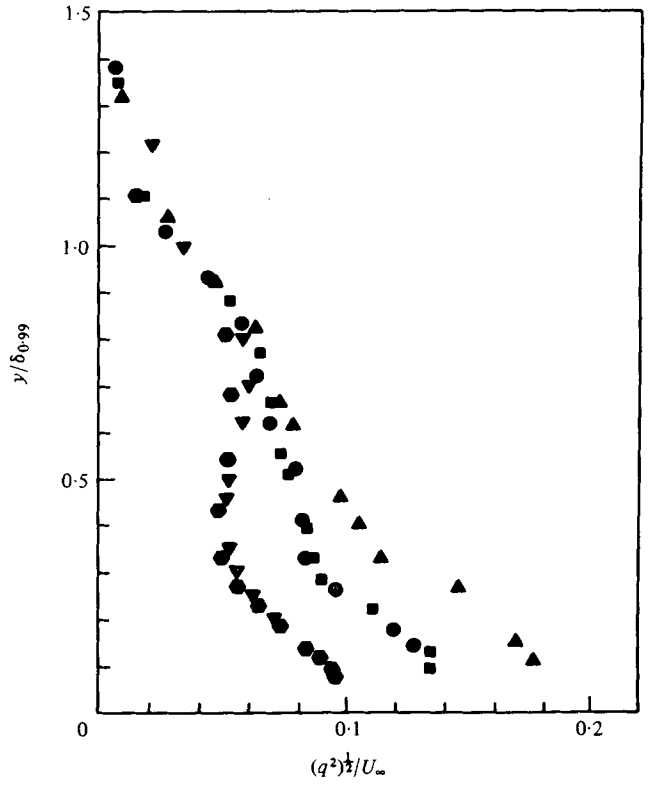

FIGURE 12. Spanwise-averaged turbulent kinetic-energy profiles for $M = 0{\cdot}5$; $U_\infty = 16{\cdot}7$ m s^{-1}. ●, $x = 148$; ▲, $x = 168$; ■, $x = 188$; ▼, $x = 214$; ●, $x = 256$.

is a fair similarity above $y/\delta = 0{\cdot}8$, in the region of undisturbed TKE. Below $y/\delta = 0{\cdot}8$, there is a rough similarity between the full-coverage region profiles and the recovery region profiles. This may mean that a state of invariance for TKE is reached in the full-coverage region which may simplify predictions of the full-coverage region and might lead to better insight into the injection process. The similarity in the recovery region may be due to the slow rate of relaxation to the two-dimensional state.

3.5. *Streamwise shear-stress profiles*

Figures 13 and 14 show the streamwise shear stress profiles at the start of the recovery region (just after the last row of injections) for $M = 0{\cdot}4$ and $M = 0{\cdot}9$, respectively. The flat-plate shear stress profiles of Klebanoff (1955) are also shown in these figures as reference lines. In both cases there is some symmetry observed for the profiles which are in symmetrical positions with respect to the centre-line. Compared to the reference shear stress, excesses are observed for the $M = 0{\cdot}4$ case, above $y/\delta \simeq 0{\cdot}2$, for all of the spanwise profiles. In general, for the $M = 0{\cdot}9$ case, however, defects can be seen when compared to the reference profiles below $y/\delta \simeq 0{\cdot}6$. Above $y/\delta \simeq 0{\cdot}6$, there are some excesses, but the magnitudes of these are less than for the $M = 0{\cdot}4$ case. This may be due to the higher shear action of the effective jet spread for the low blowing. The shear stress levels are much higher for $M = 0{\cdot}4$ than for $M = 0{\cdot}9$, as was expected from the mean velocity gradients. This is another indication of high

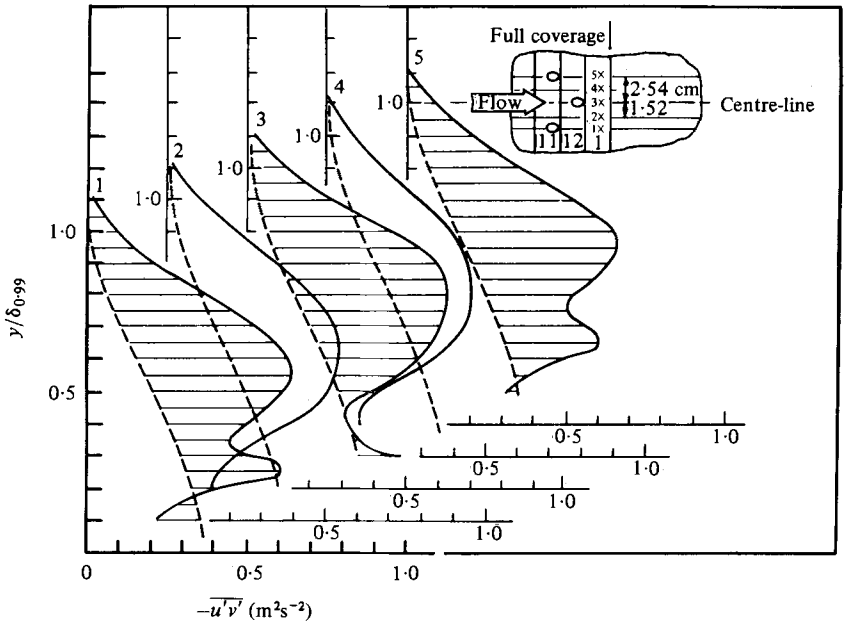

FIGURE 13. Streamwise turbulent shear stress component ($-\overline{u'v'}$) at the start of the recovery region for $M = 0{\cdot}4$; $U_\infty = 16{\cdot}5$ m s^{-1}. ——, curves through data; - - -, two-dimensional flat-plate shear stress.

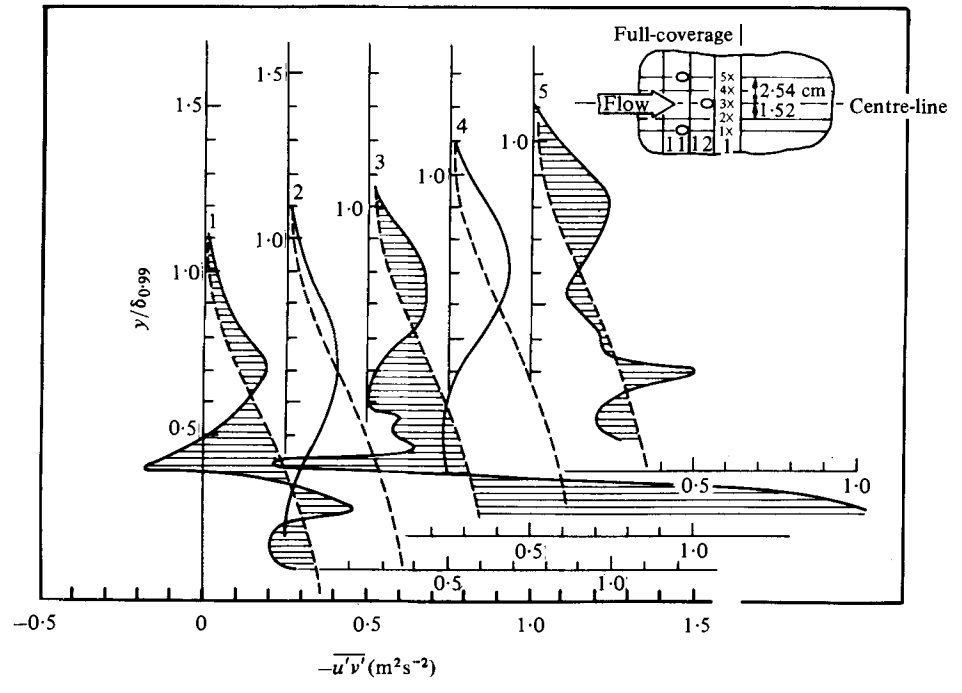

FIGURE 14. Streamwise turbulent shear stress component ($-\overline{u'v'}$) at the start of the recovery region for $M = 0{\cdot}9$; $U_\infty = 16{\cdot}7$ m s^{-1}. ——, curves through data; - - -, two-dimensional flat-plate shear stress.

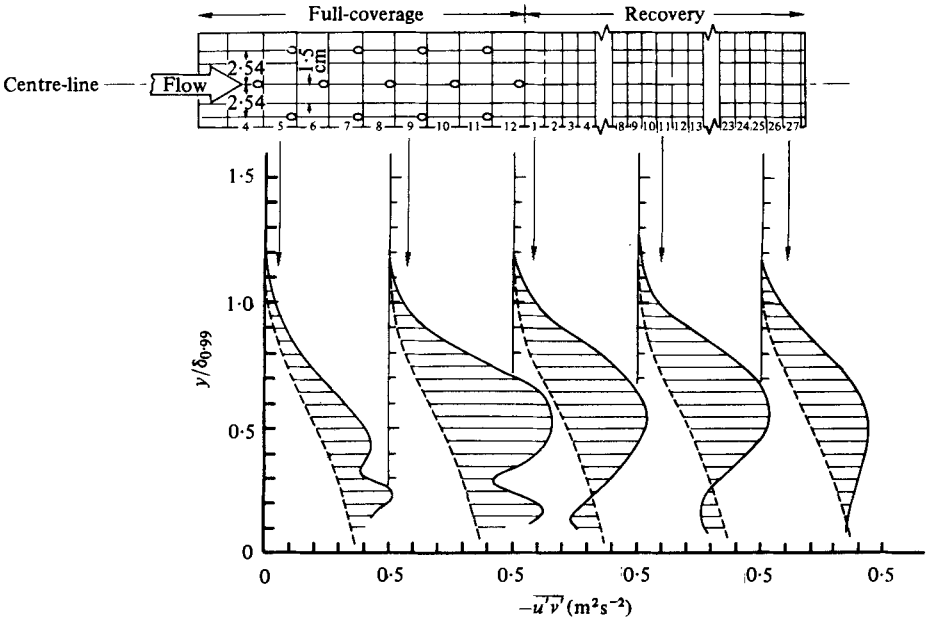

FIGURE 15. Spanwise-averaged profiles of the streamwise turbulent shear stress component for $M = 0{\cdot}4$; $U_\infty = 16{\cdot}5$ m s^{-1}. ——, curves through data; – – –, two-dimensional flat-plate shear stress.

turbulence mixing for the low blowing. The extremely high shear stress next to the wall in the central profile for the $M = 0{\cdot}9$ case must be due to the separated jet, which creates a high shear and vortex region there.

Some negative shear stresses can be seen for $M = 0{\cdot}9$ in the central (no. 3) and side profiles (nos. 1 and 5) due to the separation of jets. These negative shear stress regions occur close to the points of negative streamwise mean velocity gradients. It appears that $-\overline{u'v'}$ is more or less following the direction of $\partial\overline{U}/\partial y$. Regions where the shear stress is close to zero can be seen in the intermediate profiles (nos 2 and 4) next to the wall. These correspond to the regions where $\partial\overline{U}/\partial y = 0$, from the mean velocity profiles.

Another indication of the jet separation from the surface for $M = 0{\cdot}9$ is the highly disturbed region of shear stress in the central profile extending up to $y/\delta \simeq 0{\cdot}5$ (about $y \simeq 3$ cm or three hole diameters). This is the penetration distance for the last row of injections. In fact, the same disturbed region can also be observed in the side profiles because of the jets injected one row before. However, the profiles in the middle lanes are very smooth and do not show any sign of disturbance. They also indicate a low level of turbulence for the $M = 0{\cdot}9$ case.

Figure 15 shows spanwise-averaged, streamwise shear stress profiles at five streamwise positions for $M = 0{\cdot}4$. The flat-plate shear stress profiles are also shown for comparison. In the full-coverage region the profiles grow fuller in the downstream direction as the injection effects diffuse outwards. In the recovery region, the relaxation process is quite slow. The shear stress levels are much higher in comparison to the reference values at each station, indicating high turbulent mixing.

Figure 16 shows spanwise-averaged, streamwise shear stress profiles at the start of the recovery region, as well as at the two recovery region stations for $M = 0{\cdot}9$. As

6. Summary

In this paper experimental data were presented for convective heat transport in horizontal layers of ^{4}He gas which were heated from below. The convection cell had cylindrical symmetry, and the aspect ratio $\Gamma \equiv D/2h$ (D = diameter, h = height) was equal to 5·4. By choosing different temperatures and pressures, the extent Q of departures of the system from the approximation of Oberbeck (1879) and of Boussinesq (1903) was varied. The results were analysed in terms of the theoretical predictions by Busse (1967). None of the measurements revealed the existence of the predicted inverted bifurcation at R_c which is expected to be associated with the flow of hexagonal symmetry near R_c. Instead, the Nusselt number was rounded over a narrow range of R. We attribute this to imperfections in the geometry of the cell. For the maximum value of Q achieved during the experiment, the predicted range of stability of hexagonal flow fell within the rounded region, and therefore the data do not give any information about the existence of the inverted bifurcation.

Outside the rounded region, the results for $N(R)$ were fitted to a polynomial in $\epsilon \equiv R/R_c - 1$. This fit yielded estimates of R_c and of the initial slope N_1 of N *vs.* R. It was found that both N_1 and R_c were independent of Q if R was evaluated at the static temperature T_{s0} at the midplane of the cell. This result agrees with the prediction by Busse (1967). In order to show that only a fit using $R(T_{s0})$ gives Q-independent values of R_c and N_1, the analysis was carried out also using $R(T_2)$, where T_2 is the temperature at the cold end of the cell. In that case, both R_c and N_1 were found to be strongly Q-dependent.

The values found for R_c in the limit $Q = 0$ agreed within experimental uncertainties with the theoretical result for a laterally finite system with $\Gamma = 5{\cdot}4$ (Charlson & Sani 1970), but had insufficient accuracy to distinguish between the finite Γ value of R_c and the one appropriate for $\Gamma = \infty$. The initial slope N_1 was less than the theoretical value for $\Gamma = \infty$ (Schlüter *et al.* 1965), but consistent with measurements for other finite aspect ratios (Behringer & Ahlers 1977).

REFERENCES

Ahlers, G. 1971 Heat capacity near the superfluid transition in ^{4}He at saturated vapor pressure. *Phys. Rev.* A **3**, 696–716.

Ahlers, G. 1974 Low temperature studies of the Rayleigh–Bénard instability. *Phys. Rev. Lett.* **33**, 1185–1188.

Ahlers, G. 1975 The Rayleigh–Bénard instability at helium temperatures. In *Fluctuations. Instabilities, and Phase Transitions* (ed. T. Riste), pp. 171–193. Plenum.

Ahlers, G. 1978 Thermal conductivity of ^{4}He vapor as a function of density. *J. Low Temp. Phys.* **31**, 429–439.

Becker, E. W., Misenta, R. & Schmeissner, F. 1954*a* Viscosity of gaseous He^3 and He^4 between 1·3 °K and 4·2 °K. *Phys. Rev.* **93**, 244.

Becker, E. W., Misenta, R. & Schmeissner, F. 1954*b* Die Zähigkeit von gasförmigem He^3 und He^4 zwischen 1·3 °K und 4·2 °K. *Z. Phys.* **137**, 126–136.

Behringer, R. P. & Ahlers, G. 1977 Heat transport and critical slowing down near the Rayleigh–Bénard instability in cylindrical containers. *Phys. Lett.* A **62**, 329–331.

Boussinesq, J. 1903 *Théorie Analytique de la Chaleur*, vol. 2. Paris: Gauthier–Villars.

Busse, F. H. 1962 Dissertation, University of Munich. [English translation by S. H. Davis, *Rand Rep. LT*-66-19, Rand Corp., Santa Monica, California.

As was seen earlier, five profiles were taken at the first and last full-coverage stations and three profiles at the second station. Results of spanwise averaging showed that three profiles were not enough to obtain a good spanwise average, since this process gave more weight than was proper to the central profile. Therefore, for the profiles at $x = 168$ cm (second full-coverage region station), little importance is attached to the results of spanwise averaging near the wall, when the spanwise profiles differ significantly from each other due to the injection. However, spanwise averages obtained from five profiles appear to represent the physics adequately. The spanwise-averaged profiles of mean velocity and TKE at the start of the recovery region bear a strong resemblance (at least from the standpoint of qualitative tendencies) to the profiles in the recovery region, where no spanwise averaging was done because all the spanwise profiles are the same. From this it can be concluded that the physical averaging process taking place in the flow coincides reasonably with the spanwise averaging of five profiles here.

3.7. *On the three-dimensionality of the flow field*

The three-dimensionality of the flow field is limited to the close vicinity of jets; elsewhere, the flow has a strongly preferred direction. Elaboration follows in §§ 3.8 and 3.9. Space did not permit plotting all the data (such as the components of the mean velocity and Reynolds stress tensor) at every measurement location. Some interesting representative data of this nature are given, however, as an aid to understanding the three-dimensionality and its implications for heat transfer.

3.8. *The $\overline{V}$ and $\overline{W}$ components of the mean velocity*

Figure 17 shows the $\overline{V}$ component of the mean velocity after the last row of injection for several spanwise locations for the case of $M = 0{\cdot}4$. Together with the $\overline{V}$, the flow angle between $\overline{U}$ and $\overline{V}$, γ, is also shown. Only the profiles on one side of the centre-line are plotted because of symmetry. As expected, because of the in-line jet, the highest $\overline{V}$ occurs in the centre-line profile at the point next to the wall. The smallest $\overline{V}$ values occur in the intermediate profile, which has no jet in line with it. It is significant that the direction of $\overline{V}$ depends on the profile position. At the central and side positions, $\overline{V}$ is in the positive direction (towards the free stream), whereas for the intermediate profile it is in the negative direction. The fluid is pushed upwards by jets at the position in line with them and is entrained towards the wall in between. Maximum values of $\overline{V}$ occur near the wall, reaching approximately 8 % of the free-stream velocity, whereas in most of the boundary layer they are only from 0 to 4 % of the free-stream velocity. The largest flow angle is about 10° and occurs next to the wall. The flow angles get smaller rapidly as the distance from the wall increases.

Figure 18 shows the $\overline{V}$ component of mean velocity after the last row of injection at several spanwise locations, for $M = 0{\cdot}9$. The observations for $M = 0{\cdot}4$ also apply here qualitatively. Quantitatively, the values of $\overline{V}$ are higher because of the higher rate of blowing – there is a larger drift towards the wall in the middle lanes. This is evidence of the strong role which entrainment must play in the heat transfer for high blowing ratios.

The largest value of $\overline{V}$ is around 16 % of the free stream. The largest flow angle is about 12°.

Figure 19 shows the $\overline{W}$ component for $M = 0{\cdot}4$ at the same streamwise location as

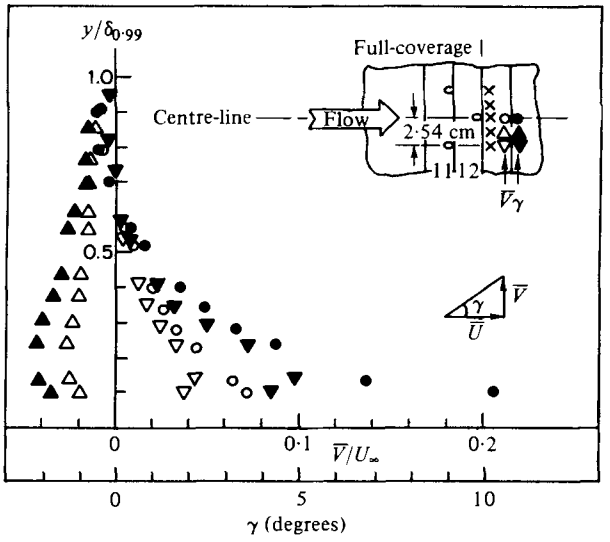

FIGURE 17. The $\overline{V}$ component of the mean velocity at the start of the recovery region for $M = 0{\cdot}4$; $U_\infty = 16{\cdot}5$ m s^{-1}.

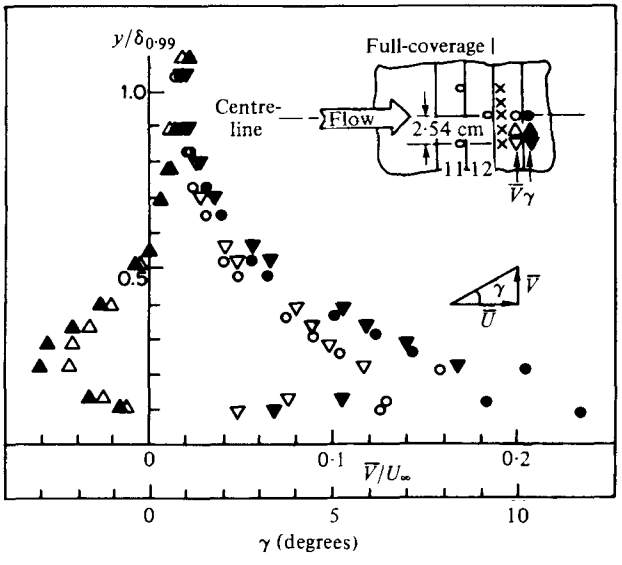

FIGURE 18. The $\overline{V}$ component of the mean velocity at the start of the recovery region for $M = 0{\cdot}9$; $U_\infty = 16{\cdot}7$ m s^{-1}.

the $\overline{V}$ components. An additional spanwise profile on the other side of the centre-line is also shown. The $\overline{W}$ component is not symmetric but, except for a few points near the wall, the $\overline{W}$ values are all small (1–3 % of the U_∞). The flow angles between $\overline{U}$ and $\overline{W}$, β, are also plotted on the same figure. Generally, $\overline{V}$ and $\overline{W}$ values for the $M = 0{\cdot}4$ case are small enough so that describing the spanwise-averaged flow as a two-dimensional boundary layer is a valid approximation.

Figure 20 shows the $\overline{W}$ component for $M = 0{\cdot}9$. The profile locations are the same as on figure 19. There is no preferred direction of the $\overline{W}$, and the values are smaller

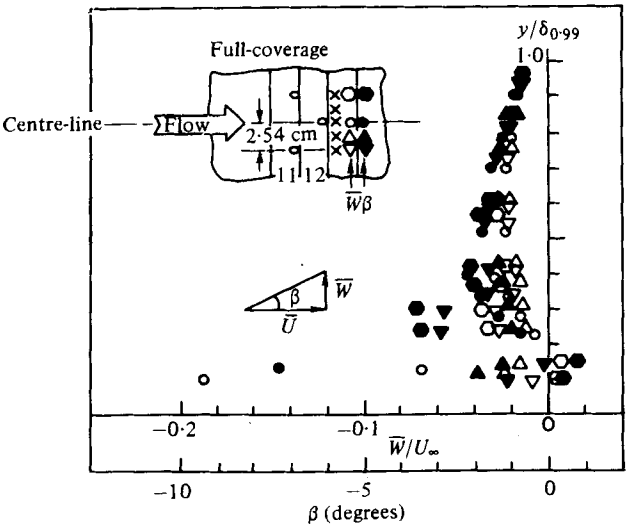

FIGURE 19. The $\overline{W}$ component of the mean velocity at the start of the recovery region for $M = 0{\cdot}4$; $U_\infty = 16{\cdot}5$ m s^{-1}.

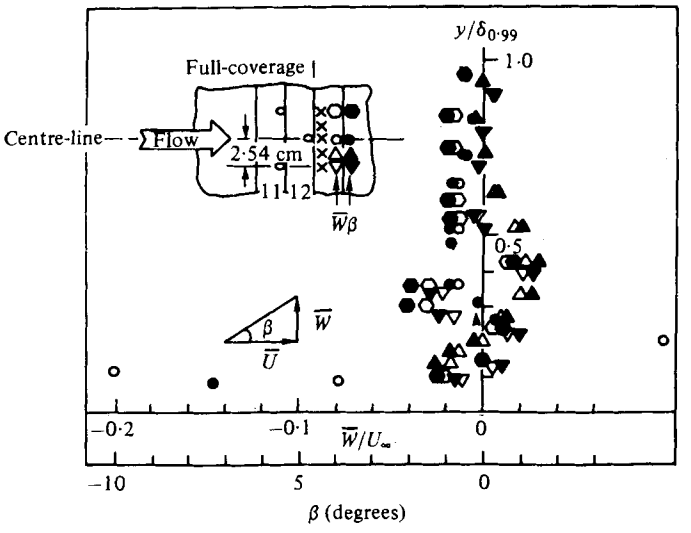

FIGURE 20. The $\overline{W}$ component of the mean velocity at the start of the recovery region for $M = 0{\cdot}9$; $U_\infty = 16{\cdot}7$ m s^{-1}.

than those for $M = 0{\cdot}4$. This is because of the low spanwise gradients in the streamwise mean velocity as compared to the low-blowing case. The low $\overline{W}$ values support both the spanwise-averaging concept and the argument concerning weak three-dimensionality, except perhaps very close to the wall, where $\overline{W}$ values are about $\pm 2\,\%$ of the U_∞.

The large and highly disturbed values of $\overline{V}$ and $\overline{W}$ near the wall for $M = 0{\cdot}9$ in the central profile are indications of vortices created by the separated jet.

In both cases of blowing, the angle range of the flow field is entirely suitable for measurements, within a good accuracy, of most of the turbulence quantities with the

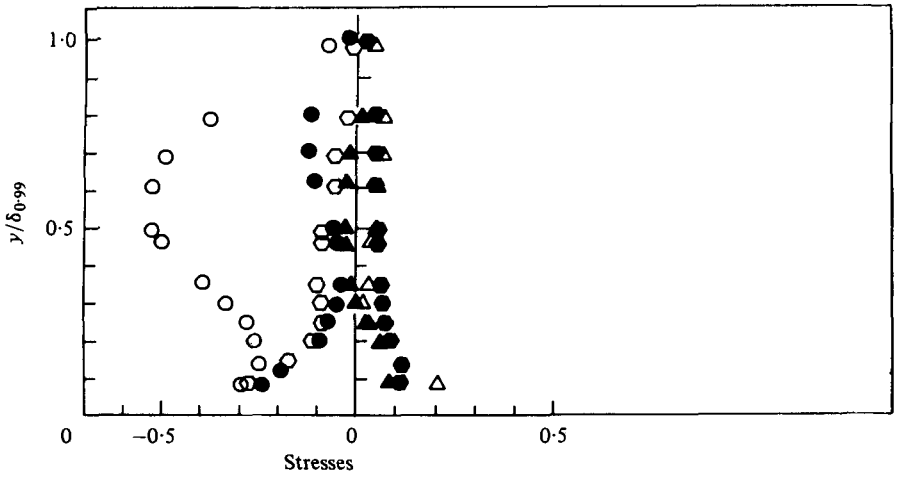

FIGURE 21. Reynolds shear stresses at the first recovery-region station, $x = 214$ cm. Open symbols are for $M = 0{\cdot}4$, $U_\infty = 16{\cdot}5$ m s^{-1}; solid symbols are for $M = 0{\cdot}9$, $U_\infty = 16{\cdot}7$ m s^{-1}. ○, $\overline{u'v'}$ (m^2 s^{-2}); △, $\overline{u'w'}$ (m^2 s^{-2}); ⬡, $\overline{v'w'}$ (m^2 s^{-2}).

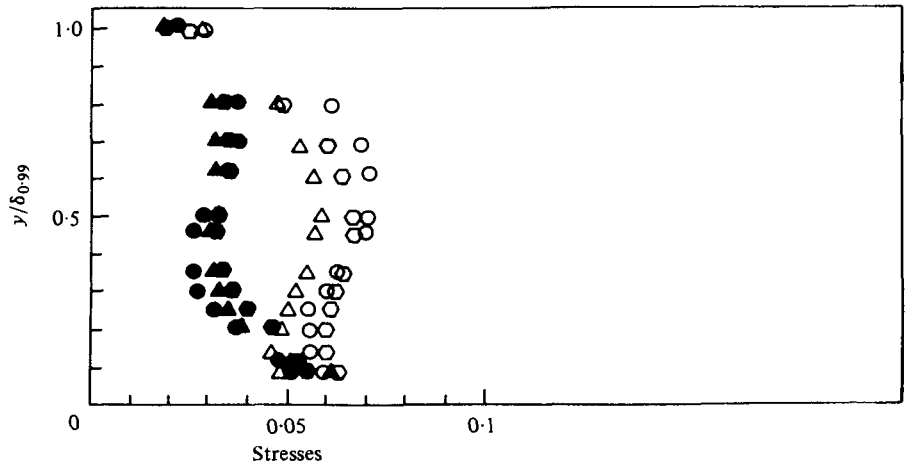

FIGURE 22. Reynolds normal stresses at the first recovery-region station, $x = 214$ cm. Open symbols are for $M = 0{\cdot}4$; $U_\infty = 16{\cdot}5$ m s^{-1}; solid symbols are for $M = 0{\cdot}9$, $U_\infty = 16{\cdot}7$ m s^{-1}. ○, $(\overline{u'^2})^{\frac{1}{2}}/U_\infty$; △, $(\overline{v'^2})^{\frac{1}{2}}/U_\infty$; ⬡, $(\overline{w'^2})^{\frac{1}{2}}/U_\infty$.

triaxial wire system (Yavuzkurt *et al.* 1977), except perhaps at the point next to the wall just downstream of a jet for the $M = 0{\cdot}9$ case.

3.9. *Reynolds stresses*

Figure 21 shows the Reynolds shear stresses for the first station in the recovery region (27 hole diameters downstream of the last row of injection) for $M = 0{\cdot}4$ and $0{\cdot}9$. These profiles are given to show a sample of the data; the rest can be found in Yavuzkurt *et al.* (1977).

The $(\overline{u'v'})$ component of shear stress for $M = 0{\cdot}4$ is significantly higher than for the others. The $(\overline{u'w'})$ and $(\overline{v'w'})$ components are almost one order of magnitude smaller

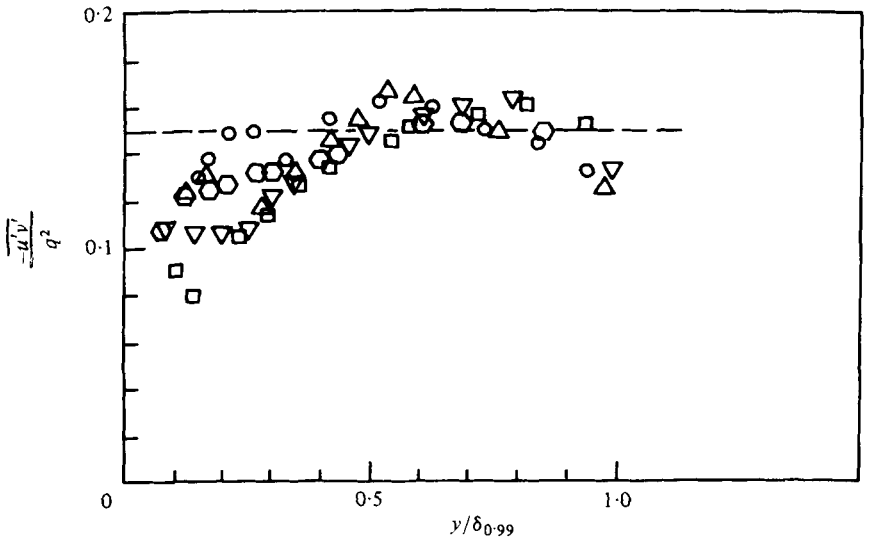

FIGURE 23. Spanwise-averaged stress–energy ratio for $M = 0{\cdot}4$; $U_\infty = 16{\cdot}5$ m s^{-1}. ○, $x = 148$; △, $x = 168$; □, $x = 188$; ▽, $x = 214$; ⬡, $x = 256$. — —, flat plate value.

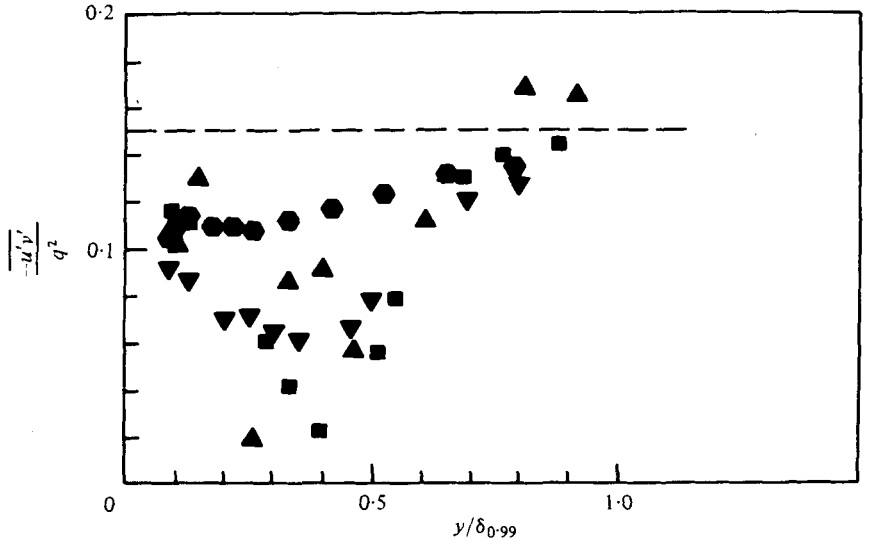

FIGURE 24. Spanwise-averaged stress–energy ratio for $M = 0{\cdot}9$; $U_\infty = 16{\cdot}7$ m s^{-1}. ▲, $x = 168$; ■, $x = 188$; ▼, $x = 214$; ⬢, $x = 256$. — —, flat-plate value.

than $(\overline{u'v'})$, except for a few points near the wall. This indicates a return to two-dimensionality for the stress field.

All of the shear stress values for $M = 0{\cdot}9$ are low in comparison to $M = 0{\cdot}4$, as expected, with the exception of $(\overline{u'v'})$ near the wall, which is high (still remembering its upstream history).

Figure 22 shows the normal Reynolds stresses at the same station as in figure 21 for $M = 0{\cdot}4$ and $M = 0{\cdot}9$. Again, the general observation is of the low turbulence level of $M = 0{\cdot}9$ in the outer region. The two cases also differ in that the data for

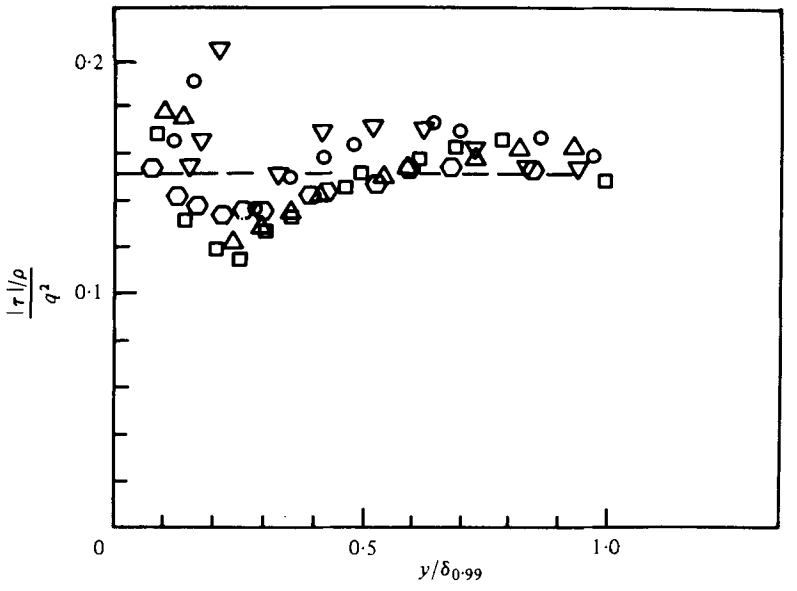

FIGURE 25. Spanwise-averaged three-dimensional stress–energy ratio for $M = 0{\cdot}4$; $U_\infty = 16{\cdot}5\,\mathrm{m\,s^{-1}}$. ▽, $x = 148$; ○, $x = 168$; △, $x = 188$; □, $x = 214$; ⬡, $x = 256$. – – –, flat plate.

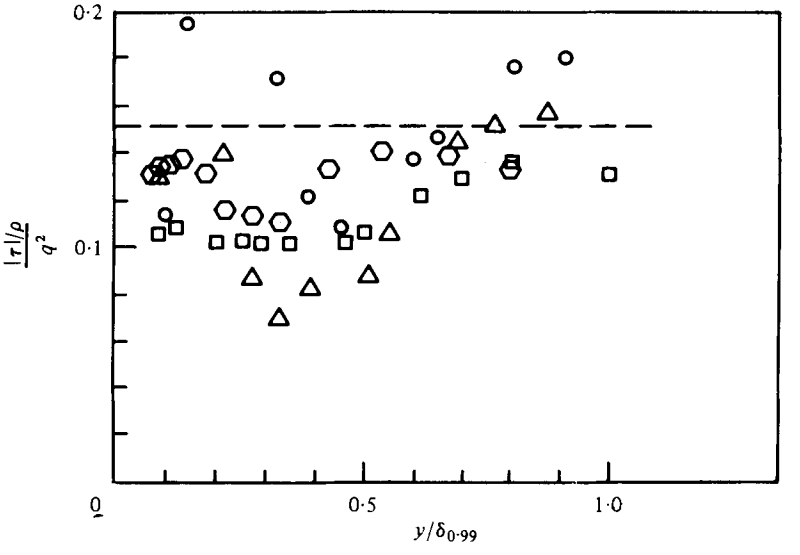

FIGURE 26. Spanwise-averaged three-dimensional stress–energy ratio for $M = 0{\cdot}9$; $U_\infty = 16{\cdot}7\,\mathrm{m\,s^{-1}}$. ○, $x = 168$; △, $x = 188$; □, $x = 214$; ⬡, $x = 256$. – – –, flat plate.

$M = 0{\cdot}9$ are nearly isotropic, with all the normal stress components very close in magnitude. This distribution may be attributed to the flat mean velocity profiles and the small spanwise gradients in the $M = 0{\cdot}9$ case; production has dropped.

3.10. *Correlation coefficients*

Figure 23 shows the spanwise-averaged stress–energy ratio ($-\overline{u'v'}/q^2$) for $M = 0{\cdot}4$ at five streamwise stations. The flat-plate value (0·15) is also given in the same figure for comparison (taken from Hinze 1975). The values near the wall are smaller than the flat-plate values, because of the disturbance caused by the injection there. The values reach the two-dimensional level above $y/\delta \simeq 0{\cdot}5$, where the jet effects are weak. Recovery to the two-dimensional values near the wall can be observed in the recovery-region stations.

The first profile after three rows of blowing does not show the large area of low stress–energy ratio shown in the other full-coverage region profiles. This must be because the effects of injection have not yet penetrated that far.

Figure 24 shows the same profiles for $M = 0{\cdot}9$. A much larger area of reduced and disturbed stress–energy ratio is observed, attributed to the deeper jet penetration; otherwise the same observations can be made for this case as in $M = 0{\cdot}4$.

Figures 25 and 26 show the spanwise-averaged three-dimensional stress–energy ratio ($|\tau|/\rho)/q^2$, for $M = 0{\cdot}4$ and $M = 0{\cdot}9$, respectively. The shear stress

$$\tau = (\overline{u'v'}^2 + \overline{u'w'}^2 + \overline{v'w'}^2)^{\frac{1}{2}}.$$

Since there is some three-dimensionality in the flow field, it was thought that it would be interesting to see the effect of three-dimensionality. Figure 25 shows that the total stress–energy ratio lies closer to the two-dimensional value than $-u'v'/q^2$, except for a few points near the wall. This suggests that the value of 0·15 may not be restricted to two-dimensional boundary layers, but may be useful in weakly three-dimensional flow such as this one. The same observations can be made for $M = 0{\cdot}9$, also, except that the effect of high blowing still shows itself in large disturbances.

Figure 27 shows the correlation coefficient, $-\overline{u'v'}/(\overline{u'^2})^{\frac{1}{2}}(\overline{v'^2})^{\frac{1}{2}}$, for both blowing ratios at the two recovery-region stations. The flat-plate value (0·45) of the correlation coefficient is also shown for comparison (Schlichting 1968). Again, for low blowing, the values are much closer to the flat-plate value than for high blowing. The effect of the injection can be observed near the wall in the form of decreased correlation coefficients for both cases. Reversion to the two-dimensional flat-plate state can be seen in the downstream direction for both blowing ratios.

3.11. *Mixing length*

The mixing length can be obtained using Prandtl's (1925) definition,

$$l = \frac{(-\overline{u'v'})^{\frac{1}{2}}}{(\partial U/\partial y)}. \tag{3}$$

Figures 28 and 29 show the mixing length obtained from the shear stress and the mean velocity data using the above formula in the recovery region for $M = 0{\cdot}4$ and 0·9. The same figures also show the mixing-length profile for a two-dimensional flat-plate boundary layer (from Escudier 1966). An augmented mixing-length region is observed at the station just after the last row of blowing ($x = 188$ cm) for both cases. This augmentation is a result of the injection process, which creates shear stresses as well as regions of low $\partial U/\partial y$. Evidence in support of this hypothesis is found in the large region of augmentation for the $M = 0{\cdot}9$ case, where the velocity profiles are quite

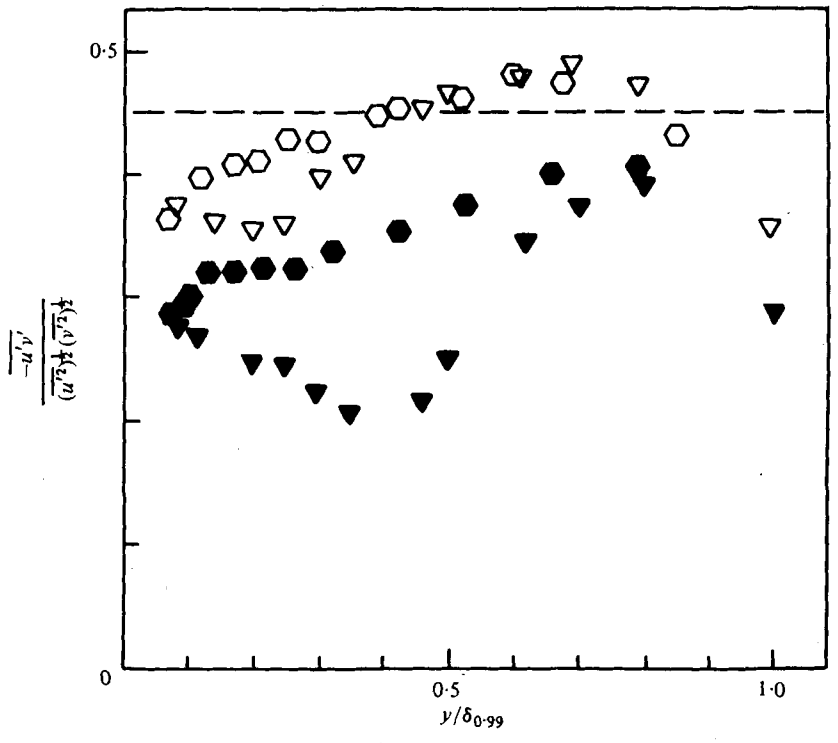

FIGURE 27. Correlation coefficient for $M = 0{\cdot}4$ (open symbols) and $M = 0{\cdot}9$ (solid symbols) at the two recovery-region stations: ▽, $x = 214$; ○, $x = 256$. – – –, flat plate.

flat. Having a high mixing length does not always imply a high rate of mixing; it may just be a result of definition. For example, even though low shear stress and TKE levels are observed for $M = 0{\cdot}9$ (figures 10 and 14), the height and width of the augmented region are much larger than for $M = 0{\cdot}4$. This is an indication of the inadequacy of the mixing-length models in regions with a zero mean velocity gradient. The peak in the mixing length dies out quite rapidly and is not observable in the recovery-region stations.

Another interesting point is the existence of regions of low mixing length near the wall, as compared to the two-dimensional flat-plate case. This region cannot be seen clearly for $M = 0{\cdot}4$, but is quite clear for $M = 0{\cdot}9$. Except for these two regions, the mixing length behaves like a classical flat-plate, two-dimensional mixing length.

4. Conclusion

One of the most important observations from these experiments is the peculiar dependence of TKE on the blowing ratio: high TKEs were observed for low blowing ($M = 0{\cdot}4$), low TKEs for high blowing ($M = 0{\cdot}9$). This phenomenon results from the low mean velocity gradients for high blowing (close to unity). The difference in the TKE levels has a significant effect on heat-transfer behaviour.

Based on these data, it seems that two different pairs of processes govern the heat transfer, depending on the level of blowing: for low blowing, the energy sink near the wall competes with high turbulent mixing; for high blowing, the energy sink in the

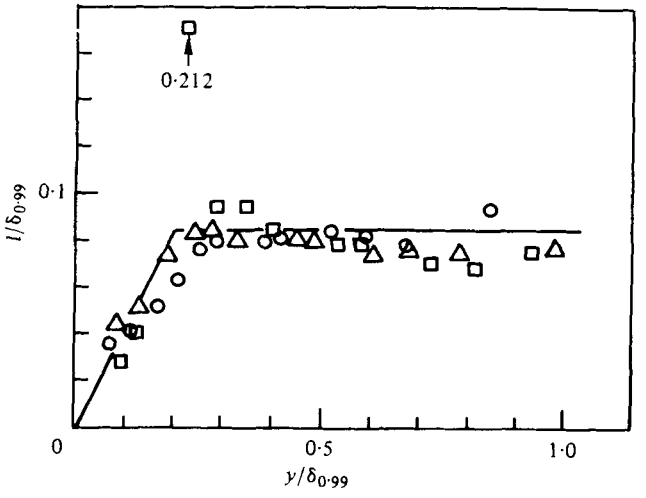

FIGURE 28. Mixing-length distribution in the recovery region for $M = 0·4$. ——, flat plate. □, $x = 188$; △, $x = 214$; ○, $x = 256$.

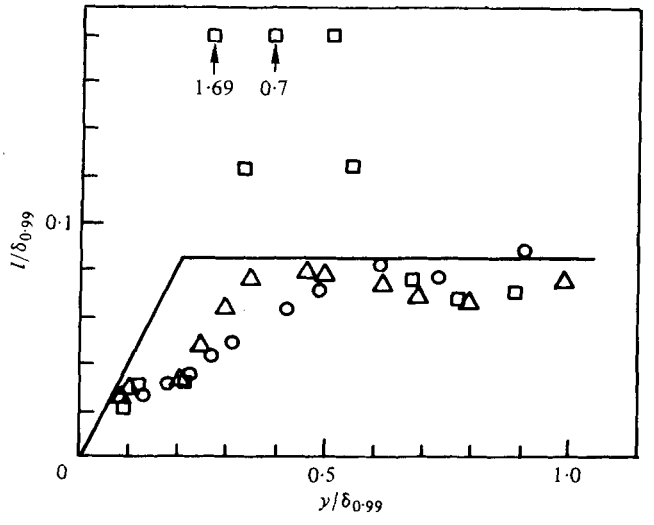

FIGURE 29. Mixing-length distribution in the recovery region for $M = 0·9$. ——, flat plate. □, $x = 188$; △, $x = 214$; ○, $x = 256$.

outer layer competes with the entrainment and convection of mainstream fluid toward the wall in the lanes between the jets. The present spanwise-averaged solution methods are not expected to predict the heat transfer well for high blowing ratios, except in a purely formal way, because they cannot handle the entrainment process and, by definition, neglect the spanwise three-dimensional flows.

This work was sponsored by the National Aeronautics and Space Administration, Lewis Research Center, under Contract NAS-314336, and by the Scientific and Technical Research Council of Turkey (Turkiye Bilimsel ve Teknik Arastirma

Kurumu), which supported the first author (Savas Yavuzkurt) during his stay at Stanford. The authors also wish to thank Dr H. Choe and Dr M. Crawford, whose apparatus was the main frame for the present work and whose careful prior studies led to this one.

REFERENCES

BERGELES, G., GOSMAN, A. D. & LAUNDER, B. E. 1975 The prediction of three-dimensional discrete-hole cooling processes. I. Laminar flow. *A.S.M.E. paper* 75-WA/HT-109.

BRUNNER, M. S. 1969 Active cooling heat protection. *J. Space Craft* **6**, no. 6.

CHOE, H., KAYS, W. M. & MOFFAT, R. J. 1975 Turbulent boundary layer on a full-coverage film-cooled surface. An experimental heat transfer study with normal injection. *N.A.S.A. Rep.* CR-2642. (Also *Stanford Univ., Mech. Engng Dept Rep.* HMT-22.)

COLLADAY, R. S. & RUSSELL, L. M. 1975 Flow visualization of discrete-hole film cooling for gas turbine applications. *N.A.S.A. Rep.* TM X-71766.

CRAWFORD, M. E. & KAYS, W. M. 1975 STAN5 – A program for numerical computation of two-dimensional internal/external boundary-layer flows. *Stanford Univ., Mech. Engng Dept Rep.* HMT-23.

CRAWFORD, M. E., KAYS, W. M. & MOFFAT R. J. 1976 Heat transfer to a full-coverage film-cooled surface with 30-deg. slant-hole injection. *Stanford Univ., Mech. Engng Dept Rep.* HMT-25.

ESCUDIER, M. P. 1966 The distribution of mixing-length in turbulent flows near walls. *Imperial College, Heat Transfer Section Rep.* TWF/TN/1.

FOSTER, R. C. & HAJI-SHEIKH, A. 1974 An experimental investigation of boundary layer heat transfer in the region of separated flow downstream of normal injection slots. *A.S.M.E. Paper* 74-HT-12.

GOLDSTEIN, R. J. 1971 Film cooling. *Adv. Heat Transfer* **7**, 269–321.

HARTNETT, J. P., BIRKEBAK, R. C. & ECKERT, E. R. G. 1961 Velocity distributions, temperature distributions, effectiveness, and heat transfer for air injected through a tangential slot into a turbulent boundary layer. *Trans. A.S.M.E.* C, *J. Heat Transfer* **83**, 293–306.

HINZE, J. O. 1975 *Turbulence*, 2nd edn, p. 643. McGraw-Hill.

KACKER, S. C. & WHITELAW, J. H. 1970 Prediction of wall-jet and wall-wake flows. *J. Mech. Engng Sci.* **12** (6), 404–420.

KLEBANOFF, P. S. 1955 Characteristics of turbulence in a boundary layer with zero pressure gradient. *N.A.C.A. Tech. note* 1247.

LAUNDER, B. E. & YORK, J. 1974 Discrete-hole cooling in the presence of free-stream turbulence and strong favorable pressure gradient. *Int. J. Heat Mass Transfer* **17**, 1403–1409.

LE BROCQ, P. V., LAUNDER, B. E. & PRIDDIN, C. H. 1971 Discrete-hole injection as a means of transpiration cooling – An experimental study. *Imperial College Rep.* HTS/71/37.

MAYLE, R. E. & CAMARATA, F. J. 1975 Multihole cooling film-effectiveness and heat transfer. *Trans. A.S.M.E.* C, *J. Heat Transfer* **97**, 534–538.

METZGER, D. E., CARPER, H. J. & WARREN, J. M. 1972 Predicted film cooling near flush slots – Comparison with experiment. *J. Aircraft* **9**, 857–863.

METZGER, D. E., TAKEUCHI, D. I. & KUENSTLER, P. A. 1973 Effectiveness and heat transfer with full-coverage film-cooling. *J. Engng Power* **95**, 180–184.

NINA, M. N. R. & WHITELAW, J. H. 1971 The effectiveness of film cooling with three-dimensional slot geometry. Gas Turbine Conference and Products Show, Houston, Texas. *A.S.M.E. Paper* no. 71-GT-11.

PRANDTL, L. 1925 Über die ausgebildete Turbulenz. *Z. angew. Math. Mech.* **5**, 136–139; and *Proc. 2nd Intern. Congr. Applied Mech., Zurich*, 1926, pp. 62–75; also *Coll. Works* II, 736–751.

RAMSEY, J. W. & GOLDSTEIN, R. J. 1971 Interaction of a heated jet with a deflecting stream. *Trans. A.S.M.E.* C, *J. Heat Transfer* **93**, 365–372.

SAMUEL, A. E. & JOUBERT, P. N. 1965 Film cooling of an adiabatic flat plate in zero pressure gradient in the presence of a hot mainstream and cold tangential secondary injection. *Trans. A.S.M.E.* C, *J. Heat Transfer* **87**, 409–419.

SCHLICHTING, H. 1968 *Boundary-Layer Theory*, 6th edn, p. 533. McGraw-Hill.

SEBAN, R. A. & BACK, L. H. 1962 Velocity and temperature profiles in turbulent boundary layers with tangential injection. *Trans. A.S.M.E.* C, *J. Heat Transfer* **84**, 45–54.

YAVUZKURT, S., MOFFAT, R. J. & KAYS, W. 1977*a* Full-coverage film cooling: three-dimensional measurements of turbulence structure and prediction of recovery region hydrodynamics. *Stanford Univ., Mech. Engng Dept Rep.* HMT-27.

YAVUZKURT, S., MOFFAT, R. J. & CRAWFORD, M. E, 1977*b* Real-time hot-wire measurements in three-dimensional flows. *Proc. 5th Biennial Symp. on Turbulence.*

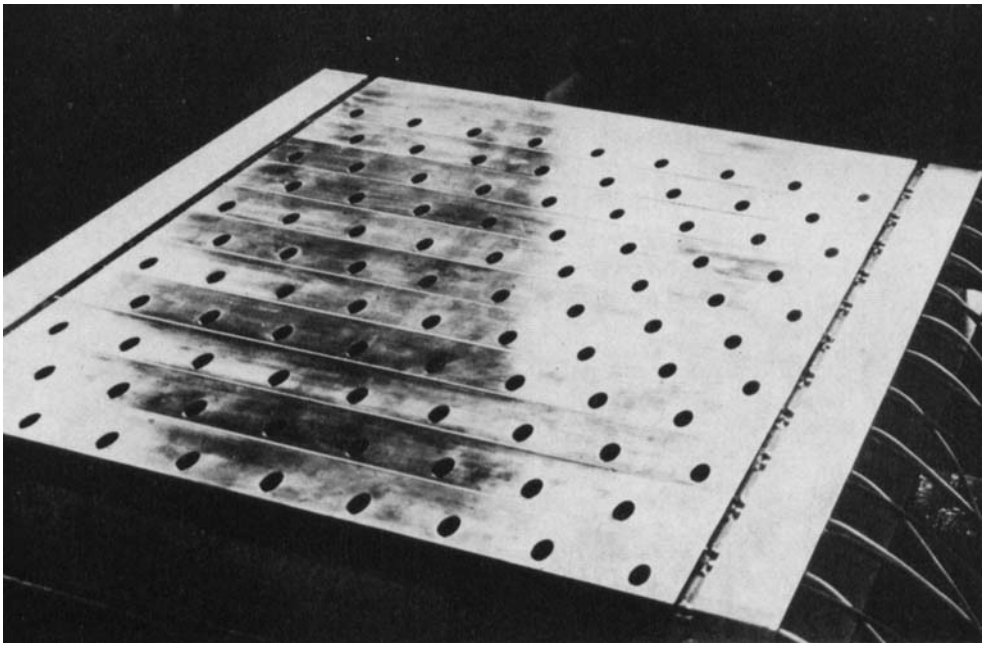

FIGURE 1. Photograph of full-coverage surface, showing staggered hole array.